Dust dynamics during the early disk evolution in the star formation process and implication for planet formation

古賀, 駿大

Dust dynamics during the early disk evolution in the star formation process and implication for planet formation

KOGA Shunta

Department of Earth and Planetary Sciences,
Graduate School of Science, Kyushu University

February 24, 2022

Abstract

Stars form in molecular cloud cores composed of gas and dust particles, and it is understood that planetary nuclei, which are dust particle aggregates, appear within the rotationally supported disks that grow in star formation processes. However, while the dynamics of dust in star formation processes have been investigated in both theoretical and observational studies, they remain poorly understood because of the dust property uncertainties. Accordingly, this study proposes a method for calculating dust particle trajectories in which dust particles are treated as Lagrangian particles. I then implement my method in a previously developed nested grid code in which the local physical quantities of gas fluid are used to calculate dust dynamics. More specifically, I perform three-dimensional (3D) magnetohydrodynamic (MHD) simulations that include dust particle trajectory calculations to investigate dust dynamics in a collapsing cloud with variously-sized dust particles. I then show that the obtained results are qualitatively and quantitatively consistent with previous studies that adopted one- or two-fluid approximations with the Eulerian approach. I also find that dust particles that satisfy $a_{\rm d} \leq 10$ μm (where $a_{\rm d}$ is the dust particle size) couple with the gas during gravitational collapse until the protostellar mass reaches about 8% of the initial cloud core mass. This coupling condition is also consistent with previous studies. Next, I show that the trajectory calculation adopted in this study is appropriate for tracing dust dynamics in star formation processes. Then, focusing on the trajectories of the dust particles in the disk, I determine that dust particles with an initial large θ (θ is the zenith angle) enter the disk from the equatorial plane rather than from the above, and that such dust particles do not spiral down into the central star even though they move in a circular motion. Furthermore, while the gas within 10 au loses its angular momentum, the gas beyond that distance receives angular momentum due to gravitational torque. Thus, dust particles that are strongly coupled with gas at a distance of around 10 au move also undergo circular motion.

Contents

1 Introduction

1.1 Gas evolution during star formation process

Stars form in molecular cloud cores composed primarily of gas via processes that have previously been thoroughly investigated in both theoretical and observational studies. For example, recent Atacama Large Millimeter/submillimeter Array (ALMA) observations have revealed significant information on star and planet formation processes (e.g., Lee et al., 2014), and have clarified my understanding of planet formation onset at the early star formation stage. In theoretical studies using three-dimensional (3D) magnetohydrodynamic (MHD) simulations, numerous researchers have investigated the early star formation stages, in which the formation processes for protostars and circumstellar disks in molecular cloud cores were clarified (e.g., Hennebelle & Fromang, 2008; Machida & Matsumoto, 2011; Masson et al., 2016; Price & Bate, 2007; Tomida et al., 2015; Tsukamoto et al., 2015; Wurster et al., 2016).

Fig. 1 shows observational results for a star-forming region. In this figure, a pseudo disk and a Keplerian disk are formed around the protostar, and a jet flows from the star. Fig. 2 shows the results of a 3D radiation MHD simulation. As can be seen in these figures, the simulation results are nearly identical to results obtained via observations.

1.2 Dust properties in star-forming regions

Although gas dynamics in star formation processes have been thoroughly investigated via 3D MHD simulations in theoretical studies, it should be noted that molecular cloud cores are also composed of dust particles, and it is currently understood that planetary nuclei, which are dust particle aggregates, appear within the rotationally supported disks during

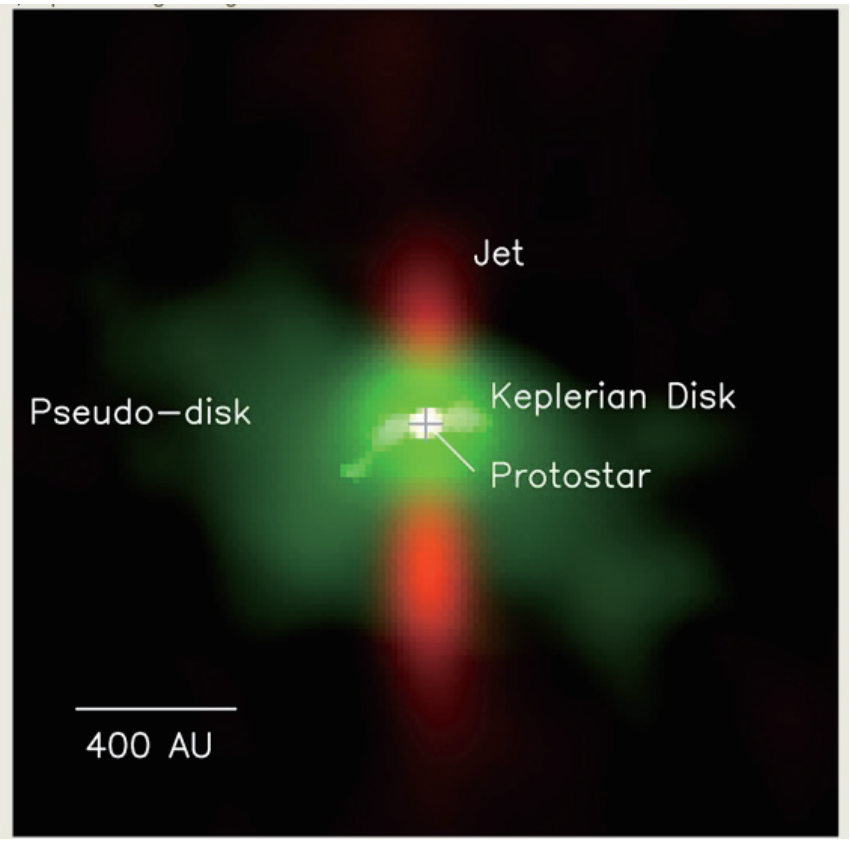

Figure 1: Observations showing the gas structure during the star formation process (Lee et al., 2014).

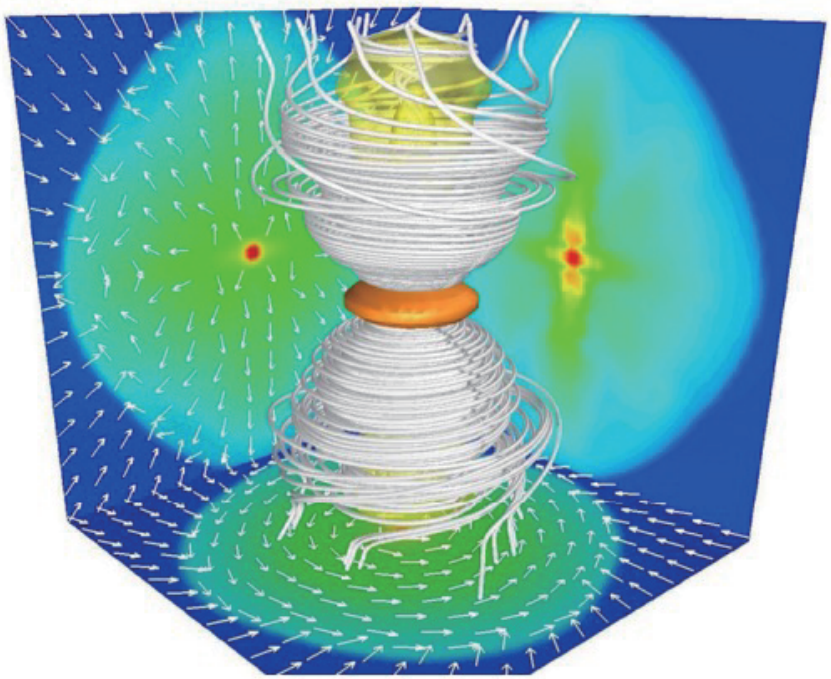

Figure 2: A 3D view of the protostellar core obtained from MHD radiation simulations (Tomida et al., 2013). The orange surface indicates the high-density region and magnetic field lines are visualized using white lines.

the star formation process. Furthermore, although dust dynamics remain poorly understood because of the uncertainties of dust properties, there are some physical quantities that can be used when determining them. One is the dust particle size (distribution). For example, based on their interstellar extinction observations, Mathis, Rumpl, & Nordsieck Mathis et al. (1977) proposed a dust particle size distribution within the range of 0.005 μm $\leq$ $a_{\rm d}$ $\leq$ 0.25 μm (hereafter referred to as the MRN distribution) that is now commonly used in star and planet formation studies.

Additionally, a very recent observation (Uehara et al., 2021) confirmed that the dust size range suggested by Mathis et al. (1977) is appropriate in the Orion A molecular cloud. On the other hand, near-infrared scattered light observations indicate that, while micron-sized dust particles exist in molecular cloud cores (Pagani et al., 2010; Steinacker et al., 2014, 2015), there is also evidence of the existence of larger-sized dust particles. For example, the dust opacity spectral index $\beta (\equiv d \ln \kappa / d \ln \nu$, where κ and ν is the opacity of the dust particles and the observational frequency, respectively) estimated from multiple-wavelength observations has been measured for both molecular cloud cores (e.g., Miettinen et al., 2012) and the gas envelopes around Class 0/I young stellar objects (YSOs) (e.g., Galametz et al., 2019; Kwon et al., 2009; Li et al., 2017; Miotello et al., 2014). These observations showed that β values in molecular cloud cores and Class 0/I objects are lower than those seen in the interstellar medium, thereby indicating the existence of (sub-)millimeter dust particles in star-forming clouds. Thus, although interstellar extinction observations imply that dust particles exist in the size range of 0.005 μm $\leq$ $a_{\rm d}$ $\leq$ 0.25 μm, other observations indicate the existence of millimeter-sized dust particles as well, which may support the possibility of dust growth in star-forming cores.

The dust-to-gas mass ratio (hereafter $f_{\rm dg}$), which is another important quantity for determining the dust properties, refers to the dust concentration relative to the gas and is usually used as a parameter in star and planet formation studies. For example, in some observational studies, the gas mass is estimated from the dust continuum emissions (e.g., Hildebrand, 1983), based on the assumption that the gas mass is proportional to the dust mass (or the intensity of the dust emissions). In some theoretical studies focusing on dust growth in a protoplanetary disk, $f_{\rm dg}$ is used as a crucial parameter for determining the initial dust mass (e.g., Brauer et al., 2008). Conventionally, $f_{\rm dg} = 0.01$ is adopted in star and planet formation studies, and the numerical value $f_{\rm dg} = 0.01$, which is supported by

interstellar extinction observations (Mathis et al., 1977), does not contradict calculations of the amount of solid matter in a solar system (Hayashi, 1981).

On the other hand, using two-dimensional (2D) MHD simulations, Beitia-Antero et al. (2021) investigated dust dynamics when large-scale filaments form just prior to the onset of star formation. They found that charged dust particles are concentrated along the high-density filaments and that $f_{\rm dg}$ is enhanced by almost an order of magnitude in such regions. Moreover, in their disk survey observations of the Lupus star-forming region, Ansdell et al. (2016) reported that the $f_{\rm dg}$ obtained from the dust continuum and CO line emissions lies in the range of 0.001 to 0.1 for protoplanetary disks. Thus, the $f_{\rm dg} = 0.01$ in the protostar formation stage just prior to planet formation has not been properly certified $f_{\rm dg} = 0.01$ in recent theoretical or observational studies. These studies seem to imply that dust particles grow in early star formation processes.

1.3 The influence of dust properties on star and planet formation process

In the section above, two dust parameters are mentioned: dust particle size and the dust-to-gas mass ratio. These parameters significantly influence star and planet formation processes. For example, dust determines the chemical abundance levels of charged species, and dust particles absorb the charged particles that are produced by collisions between neutral particles and cosmic rays, as well as the charge transfer between dust particles and ions. Dust particle sizes and the dust-to-gas mass ratio are necessary for calculating the cross-sections of the dust particles that determine the absorption rate. Since these chemical abundances are directly related to the resistivities of the non-ideal MHD effects and determine the evolution of the magnetic field, dust properties are important when considering star formation processes. Additionally, the influences of dust properties on star and circumstellar disk formation have been investigated in terms of the magnetic dissipation process in theoretical studies (Dzyurkevich et al., 2017; Koga et al., 2019; Marchand et al., 2016; Tsukamoto et al., 2020; Zhao et al., 2018, 2021, 2016). For example, Zhao et al. (2016) showed that the dust size distribution and the number of small

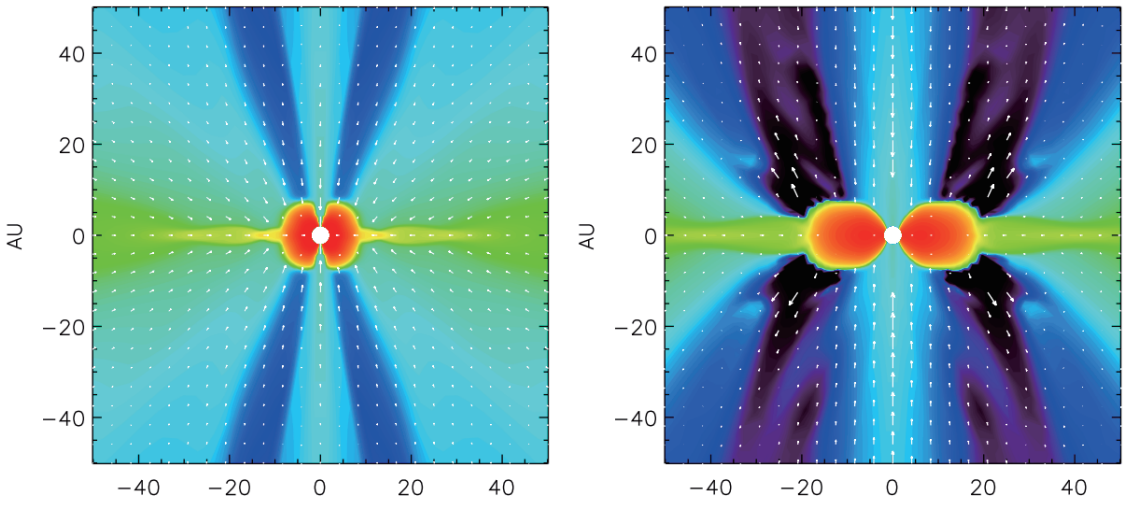

Figure 3: The 2D density colormap of the edge-on disk. The left panel shows the simulation result using MRN distribution while the right panel shows the result of the calculation using trMRN distibution defined in Zhao et al. (2016).

particles significantly affect the size and structure of a circumstellar disk. Fig. 3 shows the simulation results of Zhao et al. (2016). In the two panels, only the dust size distribution is different. The right panel shows the result using the MRN distribution to determine the resistivities of the non-ideal MHD effects while the left panel plots the result using tr-MRN distribution, which is defined by setting the minimum dust grain size $a_{\rm d,min} = 0.1$ μm. The difference in the dust size distribution produces the change of the disk radius by a factor of two.

Dust particle size is also important when studying planet formation because the increase in particle size that results from collisions is the first step toward planet formation and the growth rate is determined by how much and what size dust is present. In the classical planet formation scenario (e.g., Hayashi et al., 1985), dust growth was discussed in the minimum mass solar nebula (Hayashi, 1981). Recently, however, the expected planet-forming disks around Class II YSOs have been found to have complicated structures that include rings, gaps, and spiral arms, as reported in the Disk Substructures at High Angular Resolution (DSHARP) Project (Guzmán et al., 2018; Huang et al., 2018a,b; Isella et al., 2018; Kurtovic et al., 2018; Pérez et al., 2018). Fig. 4 shows the high-resolution observation results of the protoplanetary disks performed by the DSHARP projects. Twenty disks are observed and

substructures are confirmed in the disks. It has also been shown that the disks around Class 0/I YSOs have similar substructures (Sheehan et al., 2020). Since these observations imply that planet formation begins from the Class 0 and I stages, the planet formation scenario should be revisited and reconsidered within the star formation framework. Fig. 5 shows the observation result reported in Sheehan et al. (2020). Ring structures are confirmed in the disk. Furthermore, since star formation begins in a molecular cloud core, dust growth within collapsing cloud cores should also be considered. In other words, it is important to clarify dust particle sizes (and dust growth) as well as the dust-to-gas mass ratio in circumstellar disks around very young protostars during the main accretion phase.

1.4 Dust dynamics during the early star formation stage

Very recently, dust dynamics during the early star formation stage has been investigated in multi-dimensional simulations (Bate & Lorén-Aguilar, 2017; Lebreuilly et al., 2020; Tsukamoto et al., 2021b; Vorobyov et al., 2018). For example, Bate & Lorén-Aguilar (2017) calculated dust motion using 3D Smoothed Particle Hydrodynamics (SPH) simulations and found that dust particles with ≤ 10 μm sizes are coupled with gas during the protostellar collapse phase. Separately, Vorobyov et al. (2018) investigated dust dynamics and growth using their 2D multi-fluid simulation and showed that a region where dust particles are concentrated appears in viscous and self-gravitating disks. However, it should be noted that magnetic effects were ignored in these studies.

At present, to the best of my knowledge, only two studies have considered both effects of dust (dynamics) and magnetic fields in star formation simulations. The first, using 3D MHD simulations that include dust Lebreuilly et al. (2020), presented the conditions for decoupling dust (particle size larger than ≥ 100 μm) from gas, in which fluid approximation was adopted for calculating dust dynamics. Their results are consistent with Bate & Lorén-Aguilar (2017). The second study Tsukamoto et al. (2021b) investigated dust growth in 3D MHD simulations and considered various physical processes. Their results showed that the outflow helped dust growth and pointed out that dust particles can grow to centimeter

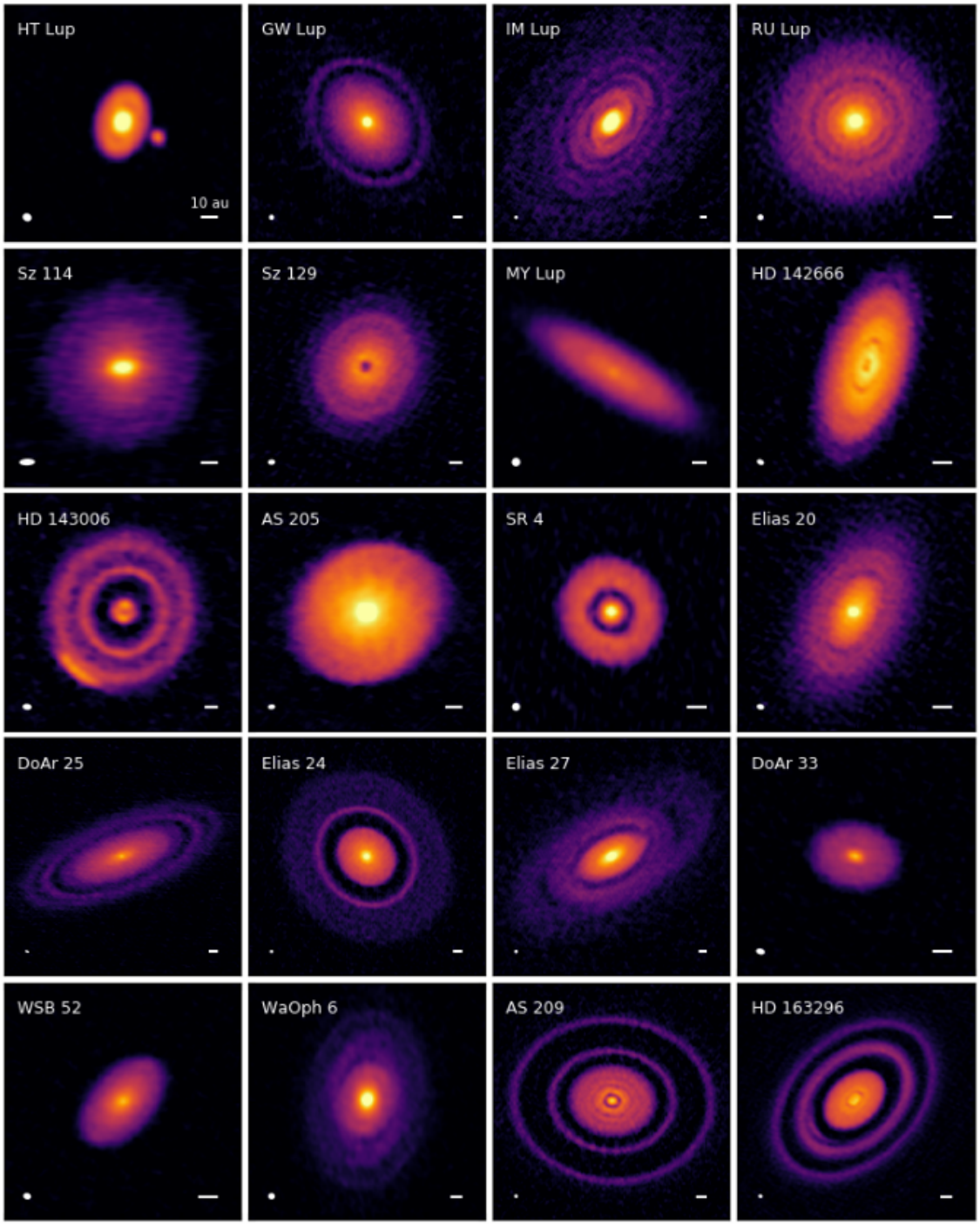

Figure 4: The high-resolution observation results of the protoplanetary disks performed by the DSHARP projects.

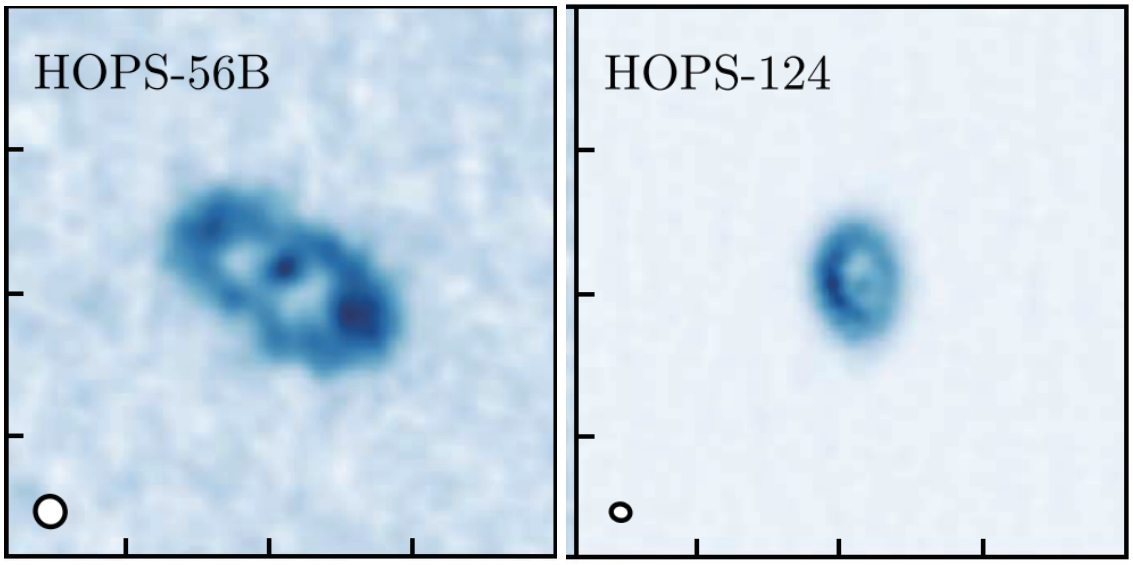

Figure 5: The observation result obtained by the VLA/ALMA Nascent Disk and Multiplicity (VANDAM) Survey reported in Sheehan et al. (2020).

(∼ cm) size. However, while both studies addressed the spatial distributions of dust in star-forming clouds, the motions of individual dust particles could not be traced because they adopted one- or two-fluid approximations (Lebreuilly et al., 2020; Tsukamoto et al., 2021b).

2 Method

2.1 Basic gas fluid equations and numerical settings

The numerical settings and initial conditions used in this study are the same as in Tomida et al. (2017) and Aso & Machida (2020). As described below, I do not include the feedback effect of dust on gas, the gas dynamics shown in this paper are identical to those provided in my previous studies and will not be discussed in detail. Instead, this subsection provides a simple explanation of the numerical settings adopted in this and previous studies, while gas evolution is calculated using our 3D MHD simulation. The basic equations are as follows:

$$\frac{\partial \rho}{\partial t} + \nabla \cdot (\rho \boldsymbol{v}) = 0, \tag{1}$$

$$\rho \frac{\partial v}{\partial t} + \rho(\boldsymbol{v} \cdot \nabla)\boldsymbol{v} = -\nabla P - \frac{1}{4\pi}\boldsymbol{B} \times (\nabla \times \boldsymbol{B}) - \rho \nabla \phi, \tag{2}$$

$$\frac{\partial \boldsymbol{B}}{\partial t} = \nabla \times (\boldsymbol{v} \times \boldsymbol{B}) + \eta_{\mathrm{O}} \nabla^2 \boldsymbol{B}, \tag{3}$$

$$\nabla^2 \phi = 4\pi G \rho, \tag{4}$$

where $\rho, \boldsymbol{v}, P, \boldsymbol{B}, \phi, and \eta_{\mathrm{O}}$ are the gas mass density, gas velocity, gas pressure, magnetic field, gravitational potential, and Ohmic dissipation resistivity coefficient, respectively. The gas pressure P is given by the barotropic equation as

$$P = c_{s,0}^2 \left(\rho + \rho_{\mathrm{cri}} \left(\frac{\rho}{\rho_{\mathrm{cri}}} \right)^{\gamma} \tanh \left(\frac{\rho}{\rho_{\mathrm{cri}}} \right)^{0.1} \right), \tag{5}$$

where $c_{s,0} = 1.6 \times 10^4$ cm s^{-1} (the sound speed corresponding to gas temperature $T = 10$ K), $\gamma = 1.4$ and $\rho_{\mathrm{cri}} = 2.0 \times 10^{-14}$ g cm^{-3} ($n_{\mathrm{cri}} = 5.0 \times 10^9$ cm^{-3}) are adopted.

The Ohmic dissipation coefficient $\eta_{\rm O}$, which was formulated in Machida et al. (2007) based on Nakano et al. (2002), is

$$\eta_{\rm O} = \frac{740}{x_e}\sqrt{\frac{T}{10{\rm K}}}\ {\rm cm^2 s^{-1}}, \tag{6}$$

where x_e represents the gas ionization degree and is calculated using the gas number density as

$$x_e = 5.7\times10^{-4}\left(\frac{n}{\rm cm^{-3}}\right)^{-1}. \tag{7}$$

Actually, the gas ionization degree x_e depends on dust properties such as dust particle size and chemical composition (e.g. Koga et al., 2019), as discussed in § 4.3. However, it should be noted that I do not consider the dependency of the ionization on the dust particle properties in this study. To perform the numerical calculations, I use the nested grid code (for details, see Machida & Hosokawa, 2013; Machida & Matsumoto, 2012; Machida et al., 2004). The cell number of each grid is set to $(x, y, z) = (64, 64, 64)$ and the grid level l was prepared from 1 to 14. The coarsest grid ($l = 1$) has a box size of $L(l = 1) = 1.96\times10^5$ au and a cell width of $h(l = 1) = 3.07\times10^3$ au, respectively. The finest grid, ($l = 14$), has $L(l = 14) = 24.0$ au and $h(l = 14) = 0.374$ au, respectively. A sink is introduced at the computational domain center (Machida et al., 2010) and I set the sink radius $r_{\rm sink}$ and threshold number density $n_{\rm sink}$ as $r_{\rm sink} = 1$ au and $n_{\rm sink} = 10^{13}$ cm^{-3}, respectively.

2.2 Dust dynamics and calculation method

Since this study aims to clarify dust dynamics in relation to gas evolution in the star formation process, I newly introduce Lagrangian dust particles into our nested grid code. In this section, I explain the method used to compute dust particle motion. Specifically, dust particles are treated as moving solid particles according to the equations of motion. In other words, gas is treated as an Eulerian fluid while dust particles are treated as Lagrangian particles. This method has an advantage when tracing Lagrangian physical quantities and understanding the evolution of size distributions, chemical reactions, and the temperatures of each particle. However, it is different from Lebreuilly et al. (2020), which calculated

dust dynamics with one fluid approach that included both gas and dust. My treatment is also different from Johansen & Youdin (2007),Bai & Stone (2010) and Flock & Mignone (2021), in which the motions of dust particles and gas fluid in the protoplanetary disk were calculated to study streaming instability, which is closely related to planet formation and can result from gas and dust interactions. Those instabilities, including the feedback (or backreaction) from dust, are not considered here because they are beyond the scope of the present work.

2.2.1 The equation of motion of dust particles

Next, I will describe the method for performing dust trajectory calculations at each time step. Since gas drag force and gas self-gravity are considered, the equation of motion for a dust particle is given by

$$\frac{d\boldsymbol{v}_{\rm d}}{dt} = -\frac{\boldsymbol{v}_{\rm d} - \boldsymbol{v}}{t_{\rm s}} + \boldsymbol{g}. \tag{8}$$

In equation (8), $t_{\rm s}$ is a timescale called the stopping time and is defined as

$$t_{\rm s} = \frac{a_{\rm d}\rho_{\rm s}}{v_{\rm th}\rho}, \tag{9}$$

where $\boldsymbol{v}_{\rm d}, a_{\rm d}, and \rho_{\rm s}$ are the dust particle velocities, dust particle size, and the dust particle material density, respectively. Meanwhile, $v_{\rm th}$ is the thermal velocity of molecular gas and is defined as $v_{\rm th} = \sqrt{\frac{8}{\pi}}c_s$, where c_s is sound speed. In this study, it is assumed that dust particles are composed of ice and thus adopt $\rho_{\rm s} = 1$ g cm^{-3}, which is the same as in Lebreuilly et al. (2020). In addition, each dust particle is assumed to be a spherical solid particle. Thus, $a_{\rm d}$ corresponds to the radius of each dust particle. Here, it should be noted that in the settings of this study, the law of gas drag varies with the dust particle size $a_{\rm d}$ and mean free path and that the dust particles move according to Epstein's law. Furthermore, using some trial calculations, I confirmed that the dust particles adopted in this study interact with the gas solely in accordance with Epstein's law. The transition between the two regimes (Epstein's and Stokes' laws) is determined by the dust particle size $a_{\rm d}$ and the mean free path $\lambda = 1/(n\sigma_{\rm mol})$, where n and $\sigma_{\rm mol} = 2.0 \times 10^{-15}$ cm^2 are the gas number density and the collisional cross section of gas molecules, respectively.

If a dust particle satisfies the condition $a_{\rm d} < \frac{9}{4}\lambda$, it obeys Epstein's law and its stopping time is given by equation (9). Otherwise, for the Stokes' law regime, the stopping time is expressed as

$$t_{\rm s} = \frac{4a_{\rm d}^2\rho_{\rm s}}{9v_{\rm th}\rho\lambda}. \tag{10}$$

Next, I introduce the sink particle and set the threshold gas number density as $n_{\rm sink} = 10^{13}$ cm^{-3}, as described in § 2.1. Since the maximum gas number density never exceeds $n_{\rm sink}$ in the whole region, there is no region that satisfies $n > 10^{13}$ cm^{-3}. Therefore, the shortest mean free path $\lambda_{\rm min}$ that appears in the calculation is

$$\lambda_{\rm min} = \frac{1}{n_{\rm sink}\sigma_{\rm mol}} \approx 50 \text{ cm}. \tag{11}$$

Since the dust particle size $a_{\rm d}$ adopted in this study is always much smaller than $\lambda_{\rm min}$ (see Table 1), these dust particles always obey the condition $a_{\rm d} < \frac{9}{4}\lambda$. Moreover, the dust particles in Epstein's law should satisfy subsonic relative motions between the dust particle and gas. However, some particles experience supersonic relative velocities during the calculation. Therefore, I use the correction term adopted in Laibe & Price (2012), which is described in §2.2.2, which means that the gas drag term can be calculated using equations (8) and (9) as described in Epstein (1924). In addition, it is assumed that the dust particles do not interact with each other.

2.2.2 Numerical implementation

To perform a trajectory calculation, it is necessary to determine the physical gas quantities $(\rho, \boldsymbol{v}, \boldsymbol{B}, \boldsymbol{g})$ at the dust particle positions of each time step. Here, $\boldsymbol{g} = -\nabla\phi$ is the gas gravitational acceleration and dust self-gravity is ignored. The local physical gas quantities are acquired from the cells surrounding the dust particle. In our nested grid code, the physical gas quantities (e.g., ρ) are defined at the center of each cell. For example, I calculate the local gas mass density $\rho_{\rm lc}$ to the position of a dust particle by linear interpolation formula as

$$\rho_{\rm lc} = \rho_1 + \frac{x_{\rm d} - x_1}{h_{\rm cell}}\Delta\rho_x + \frac{y_{\rm d} - y_1}{h_{\rm cell}}\Delta\rho_y + \frac{z_{\rm d} - z_1}{h_{\rm cell}}\Delta\rho_z, \tag{12}$$

where $h_{\rm cell}$ is the cell width, and ρ_1 is the density of the cell within which the dust particle is included. Note that the cell width is the same in each direction (or the x, y, and z directions), and I define $A = (x, y, and z)$, and $A_{\rm d}$ and A_1 as the positions of the dust particle and the cell that includes the dust particle, respectively. $\Delta\rho_A$ is defined as

$$\Delta\rho_A = S(\rho_{2,A} - \rho_1, A_{\rm d} - A_1), \tag{13}$$

where $\rho_{2,A}$ is the nearest cell in each direction to the dust particle position along the "A"-coordinate direction, and the function S is defined as

$$S(a, b) = a \times sgn(b), \tag{14}$$

where sgn is the sign function. The local quantity of $\boldsymbol{v}, \boldsymbol{B}, \boldsymbol{g}$ is calculated in the same way as for ρ, as described above. Hereafter, in this subsection, the physical gas quantities indicate those at the dust particle position taken by linear interpolation, and I describe the local physical gas quantities with subscript "lc".

To calculate dust trajectories, it is necessary to integrate equation (8). Note that $\boldsymbol{v}_{\rm lc}$ is used instead of $\boldsymbol{v}$ in equation (8). When dust is strongly coupled with gas, $\Delta t/t_{\rm s}$ is close to infinity, in which Δt is the numerical time step used in the trajectory calculation. Thus, in a strongly coupled region, the time step in the orbit (or trajectory) calculation becomes very short, which makes the calculation very difficult. To avoid this difficulty, I analytically determine the relative velocity between the dust and gas at the next time step. According to the prescription described in Laibe & Price (2014) and Tsukamoto et al. (2021a), the relative velocity time evolution equation $\Delta\boldsymbol{v} = \boldsymbol{v}_{\rm d} - \boldsymbol{v}$ is adopted. Hence, the relative velocity equation can be transformed as

$$\frac{d\Delta\boldsymbol{v}}{dt} = -\frac{\Delta\boldsymbol{v}}{t_{\rm s}} + \boldsymbol{a}_{\rm ext}, \tag{15}$$

where $\boldsymbol{a}_{\rm ext}$ is the external force term of the relative motion and is described as

$$\boldsymbol{a}_{\rm ext} = \frac{1}{\rho_{\rm lc}}\nabla P_{\rm lc} + \frac{1}{4\pi\rho_{\rm lc}}\boldsymbol{B}_{\rm lc} \times (\nabla \times \boldsymbol{B}_{\rm lc}). \tag{16}$$

Note that the external force $\boldsymbol{a}_{\rm ext}$ only operates on the gas, an not the dust. As described in §2.2.1, I use the corrected $t_{\rm s}$ to avoid supersonic relative motion, which is described as

$$t_{\rm s} = \frac{a_{\rm d}\rho_{\rm s}}{v_{\rm th}\rho}\frac{1}{\sqrt{1+\frac{9\pi}{128}\left(\frac{\Delta v}{c_s}\right)^2}}, \tag{17}$$

where $\Delta v = |\boldsymbol{v}_{\rm d} - \boldsymbol{v}_{\rm lc}|$ is the relative velocity between the dust and gas In this study, dust particles are assumed to be electrically neutral, but if dust particles are charged, they are subjected to an additional Lorentz force $\boldsymbol{f}_{\rm cd}$, where $\boldsymbol{f}_{\rm cd}$ is defined as

$$\boldsymbol{f}_{\rm cd} = \frac{Z_{\rm d}e}{m_{\rm d}}\left(\boldsymbol{E} + \frac{\boldsymbol{v}_{\rm d}\times\boldsymbol{B}}{c}\right), \tag{18}$$

where $Z_{\rm d}e, m_{\rm d}, \boldsymbol{E}, andc$ are the particle charge, particle mass, electric field, and speed of light, respectively. Since neutrally charged dust is assumed in this study, $Z_{\rm d}e$ is equal to zero. Thus, the Lorentz force term $\boldsymbol{f}_{\rm cd}$ that only charged dust particles possess is not included in equation (8) and does not appear in equation (16). Actually, equations (8)–(16) imply that neutral dust particles are subjected to a Lorentz force $(-\frac{1}{4\pi\rho}\boldsymbol{B}\times(\nabla\times\boldsymbol{B}))$ via the gas fluid. The validity of the above assumption is discussed in § 4.4.

Next, I will discuss the numerical calculation scheme. Hereafter, the superscripts n and $n+1$ stand for the physical quantities at the time t and $t+\Delta t$, respectively, where Δt is the time increment. The position of a dust particle at the next step ($t = t + \Delta t$) is calculated with second-order accuracy by

$$\boldsymbol{x}_{\rm d}^{\rm n+1} = \boldsymbol{x}_{\rm d}^{\rm n} + \boldsymbol{v}_{\rm d}^{n}\Delta t + \left(\frac{d\boldsymbol{v}_{\rm d}}{dt}\right)^{\rm n}\frac{(\Delta t)^2}{2}. \tag{19}$$

The relative velocity of the next step between the dust and gas $\Delta\boldsymbol{v}^{n+1}$ is calculated by integrating equation (15) and is described as

$$\Delta\boldsymbol{v}^{n+1} = \Delta\boldsymbol{v}^{n}e^{-\frac{\Delta t}{t_{\rm s}}} + \boldsymbol{a}_{\rm ext}^{\rm n+\frac{1}{2}}t_{\rm s}(1-e^{-\frac{\Delta t}{t_{\rm s}}}), \tag{20}$$

where

$$\boldsymbol{a}_{\rm ext}^{\rm n+\frac{1}{2}} = \frac{1}{2}\left(\boldsymbol{a}_{\rm ext}^{\rm n} + \boldsymbol{a}_{\rm ext}^{\rm n+1}\right), \tag{21}$$

is obtained with equation (16). In addition, I rewrite equation (20) using a Taylor expansion, and thus $\Delta\boldsymbol{v}^{n+1}$ is given by

$$\Delta \boldsymbol{v}^{n+1} = \begin{cases} \Delta \boldsymbol{v}^{n}\left(1 - \dfrac{\Delta t}{t_{\rm s}}\right) + \boldsymbol{a}_{\rm ext}^{\rm n+\frac{1}{2}} \Delta t & \text{for } \dfrac{\Delta t}{t_{\rm s}} < 10^{-12}, \\ \Delta \boldsymbol{v}^{n} e^{-\frac{\Delta t}{t_{\rm s}}} + \boldsymbol{a}_{\rm ext}^{\rm n+\frac{1}{2}} t_{\rm s}\left(1 - e^{-\frac{\Delta t}{t_{\rm s}}}\right) & \text{for } 10^{-12} \leq \dfrac{\Delta t}{t_{\rm s}} \leq 500, \\ \boldsymbol{a}_{0,\rm ext} t_{\rm s} & \text{for } \dfrac{\Delta t}{t_{\rm s}} > 500. \end{cases} \tag{22}$$

In the case of $\frac{\Delta t}{t_{\rm s}} < 10^{-12}$, $t_{\rm s}$ is very long, thus indicating that dust and gas are weakly coupled. To avoid double-precision rounding errors in our code, I substitute $e^{-\frac{\Delta t}{t_{\rm s}}} \approx 1 - \frac{\Delta t}{t_{\rm s}}$ in equation (20). Similarly, in the case of $\frac{\Delta t}{t_{\rm s}} > 500$, $t_{\rm s}$ is too short that the dust and gas are strongly coupled. To avoid an underflow error, I use the approximation $e^{-\frac{\Delta t}{t_{\rm s}}} \approx 0$ in equation (20). Finally, with the relative velocity at $t + \Delta t$, I can update the dust velocity as

$$\boldsymbol{v}_{\rm d}^{\rm n+1} = \boldsymbol{v}_{\rm lc}^{\rm n+1} + \Delta \boldsymbol{v}^{\rm n+1}. \tag{23}$$

The trajectory calculations explained here are conducted at every time step of gas evolution. Finally, I will explain the method for setting Δt, which is given by

$$\Delta t = {\rm Min}\Big(\Delta t_{l,\rm gas}, {\rm Min}[\Delta x_{\rm cell}/|v_{x,\rm d}|, \Delta y_{\rm cell}/|v_{y,\rm d}|, \Delta z_{\rm cell}/|v_{z,\rm d}|]\Big), \tag{24}$$

where $\Delta t_{l,\rm gas}$ is the time step of the gas fluid at the grid level "l" within which the particle exists, and is determined in the MHD calculation part. $\Delta A_{\rm cell}$ and $v_{A,\rm d}$ ($A = x, y, z$) are the cell width and dust velocity, respectively, in the "A" direction. In this study, I set $\Delta x_{\rm cell} = \Delta y_{\rm cell} = \Delta z_{\rm cell}$. The dust trajectory calculation part is synchronized with the MHD calculation part. Thus, in the case of $\Delta t < \Delta t_{l,\rm gas}$, the equations (8) - (23) are repeated to update the position and velocity of dust particles until the summation of Δt reaches $\Delta t_{l,\rm gas}$. Finally the treatment of dust particles after they fall into the sink is discussed. When a particle reaches the sink or the region within $r_{\rm sink} \leq 1$ au, I stop its trajectory calculation.

2.3 Initial conditions

2.3.1 MHD (gas fluid) part

As described in §2.1, since the initial conditions are identical to those adopted in Tomida et al. (2017) and Aso & Machida (2020), I will provide a simple overview of the initial

MHD calculation conditions here. As the initial condition, I adopt a critical Bonnor-Ebert density profile with an isothermal temperature 10 K and a central density 6×10^5 cm^{-3}. Then, the density is enhanced by a factor 2 to promote the contraction. The mass $M_{\rm cl}$ and radius $R_{\rm cl}$ of the initial cloud are $M_{\rm cl} = 1.25\,{\rm M}_\odot$ and $R_{\rm cl} = 6.13 \times 10^3$ au, respectively. A uniform magnetic field $B_0 = 5.1 \times 10^{-5}$ G and a rigid rotation $\Omega_0 = 2 \times 10^{-13}$ s^{-1} are set for the initial cloud. The ratio of thermal α_0, rotational β_0, and magnetic γ_0 energies with respect to the gravitational energy of the initial cloud are $\alpha_0 = 0.42$, $\beta_0 = 0.02$, and $\gamma_0 = 0.1$, respectively. The mass-to-flux ratio normalized by the critical value $(2\pi G^{1/2})^{-1}$ is $\mu_0 = 3$.

2.3.2 Dust part

Next, dust particles are distributed in the initial cloud. The spatial distributions of the dust particles in the spherical coordinates are described in Table 1. The radius of the initial cloud (or the Bonnor-Ebert sphere) is 6130 au, as described in §2.3.1, and the dust particles are distributed every 10 au within a range of 10–6130 au. Thus, they are placed at 613 different positions in the radial direction. In the azimuthal (ϕ) direction, the dust particles are placed every 90° within the range of ϕ = 0–270° with four different positions. In the zenith (θ) direction, they are placed every 15° within the range of θ = 0–90 ° with seven different positions. In this study, the dust particles are distributed so that the whole region of the initial cloud is spatially covered. The use of a small number of particles in the ϕ direction is sufficient for analyzing the results because an approximate level of symmetry is maintained along the z-axis during the calculation (see §3).

Six different dust particles sizes were prepared within the range of $a_{\rm d}$ =0.01–1000 μm, as described in Table 2. A wide range of the particle sizes was adopted because, as mentioned in §1, there is still no conclusive evidence regarding the sizes of dust particles in molecular cloud cores. In total, 102,984 dust particles were included in the initial cloud and calculated with the MHD calculation, in which dust particles with six different sizes (Table 2) were located at the positions listed in Table 1.

To evaluate how strongly a dust particle is initially coupled with gas, the Stokes number (St) is adopted here and defined as the stopping time normalized by a dynamical time scale. In previous studies that investigated dust evolution in a protoplanetary disk

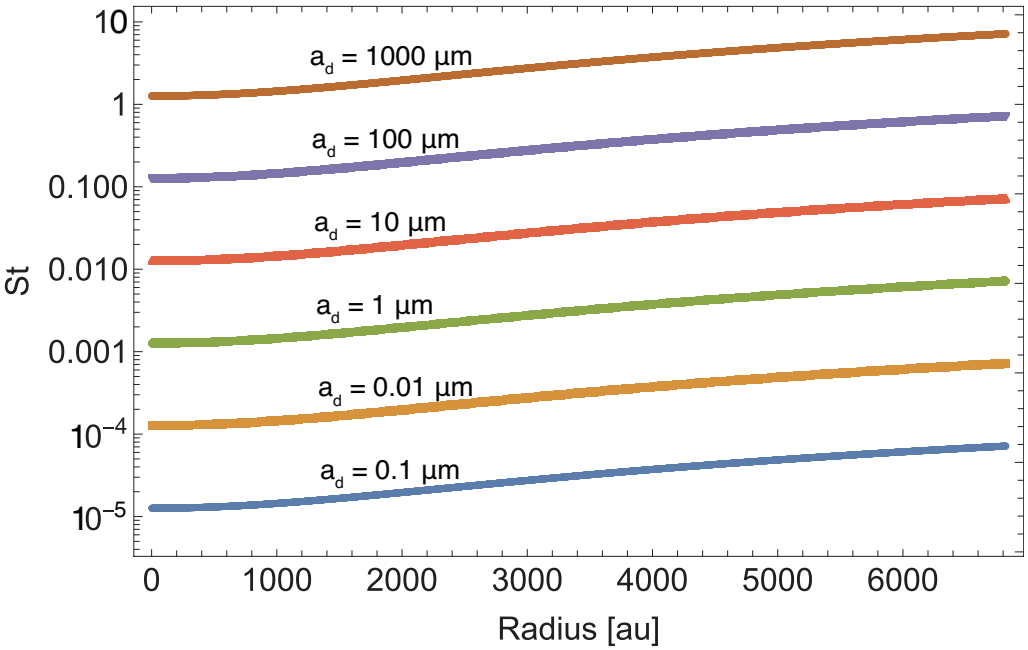

Figure 6: The initial Stokes number (t_s/t_{ff}) for dust particles distributed in the cloud versus the radial distance.

(e.g., Weidenschilling, 1977), St was normalized by the Keplerian time-scale Ω_{Kep}^{-1}, where $\Omega_{Kep} = \sqrt{GM_*/r^3}$. In this study, I focus primarily on dust motion on a scale that is larger than the (Keplerian) disk scale. Thus, instead of the Keplerian time-scale, the freefall time-scale $t_{ff} = \sqrt{3\pi/32G\rho}$ is used as the dynamical time-scale, and I describe the Stokes number as $St = t_s/t_{ff}$. Fig. 6 shows the initial Stokes number for all dust particles distributed in the Bonnor-Ebert sphere against the radius. Since t_s is proportional to the dust particle size, St becomes 10 times larger for a 10 times larger a_d. Except for dust particles with $a_d = 1000\,\mu$m, St < 1 is fulfilled within the initial cloud (or the Bonnor-Ebert sphere).

The dust particle velocity is set to be equal to the gas velocity at the initial dust particle position. In other words, all dust particles are perfectly coupled with gas at the beginning of the calculation. Fig. 6 indicates that the dust particles with $a_d = 1000\,\mu$m satisfy St > 1 and that these particles could be initially decoupled from the gas. To more realistically set the initial conditions for large particles, it would be necessary to begin the simulations from the molecular cloud core formation stage.

Table 1: Initial spatial distributions of dust particles.

Coordinates	Initial particle positions
r	10 – 6130 au (every 10 au, 613 points)
ϕ	0°, 90°, 180°, 270° (every 90°, 4 points)
θ	0°, 15°, 30°, 45°, 60°, 75°, 90° (every 15°, 7 points)

Table 2: Dust particle sizes prepared for use in my calculation.

Dust particle size $a_{\rm d}$ [μm]
0.01, 0.1, 1, 10, 100, 1000

2.4 Method for calculating the dust-to-gas mass ratio

One of the aims of this study is to calculate the spatial distribution and time evolution of the dust-to-gas mass ratio $f_{\rm dg}$. Here, the dust mass density $\rho_{\rm d}$ is required to estimate $f_{\rm dg}$, because it is defined as $f_{\rm dg} \equiv \rho_{\rm d}/\rho$ for a given spatial scale. In the calculation, however, I treat the dust as discrete particles and do not adopt a fluid approximation. Thus, $\rho_{\rm d}$ cannot be simply defined. To estimate the dust mass density, we introduce gas particles as well as dust particles and calculate how $f_{\rm dg}$ changes from the initial state by weighting the mass on both particle types (i.e., dust and gas particles). In this subsection, the weighting method used is described.

To perform the trajectory calculation for gas particles, the local physical quantities of the gas fluid, as well as dust particles, are used as described in §2.2. Although this is the same procedure used in Furuya et al. (2012), chemical reactions are not included with tracers in this study. The initial positions ($r, \phi, and \theta$) of the gas particles are set according to Table 1. Thus, seven different particles (six differently sized dust particles and one gas particle) are placed at each position.

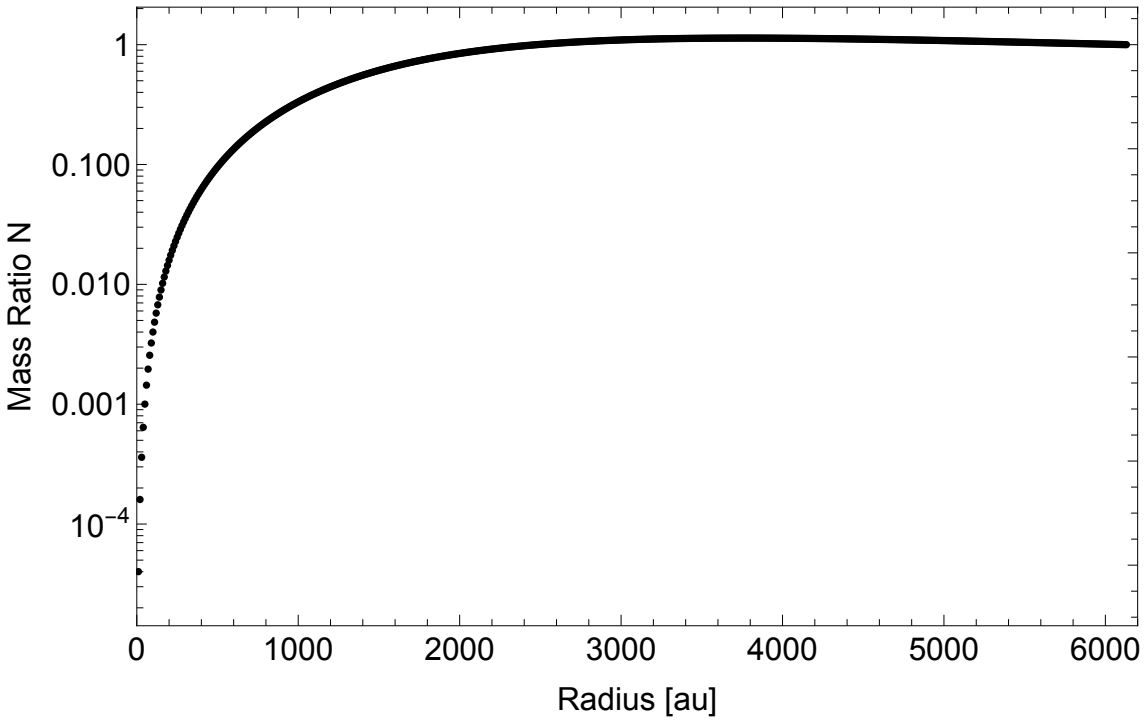

Figure 7: Shell mass ratio N of the initial cloud (or Bonnor-Ebert sphere). The ratio N is defined as each shell mass normalized by the mass of the outermost shell and is used when weighting dust and gas particles in order to derive the dust-to-gas mass ratio $f_{\rm dg}$.

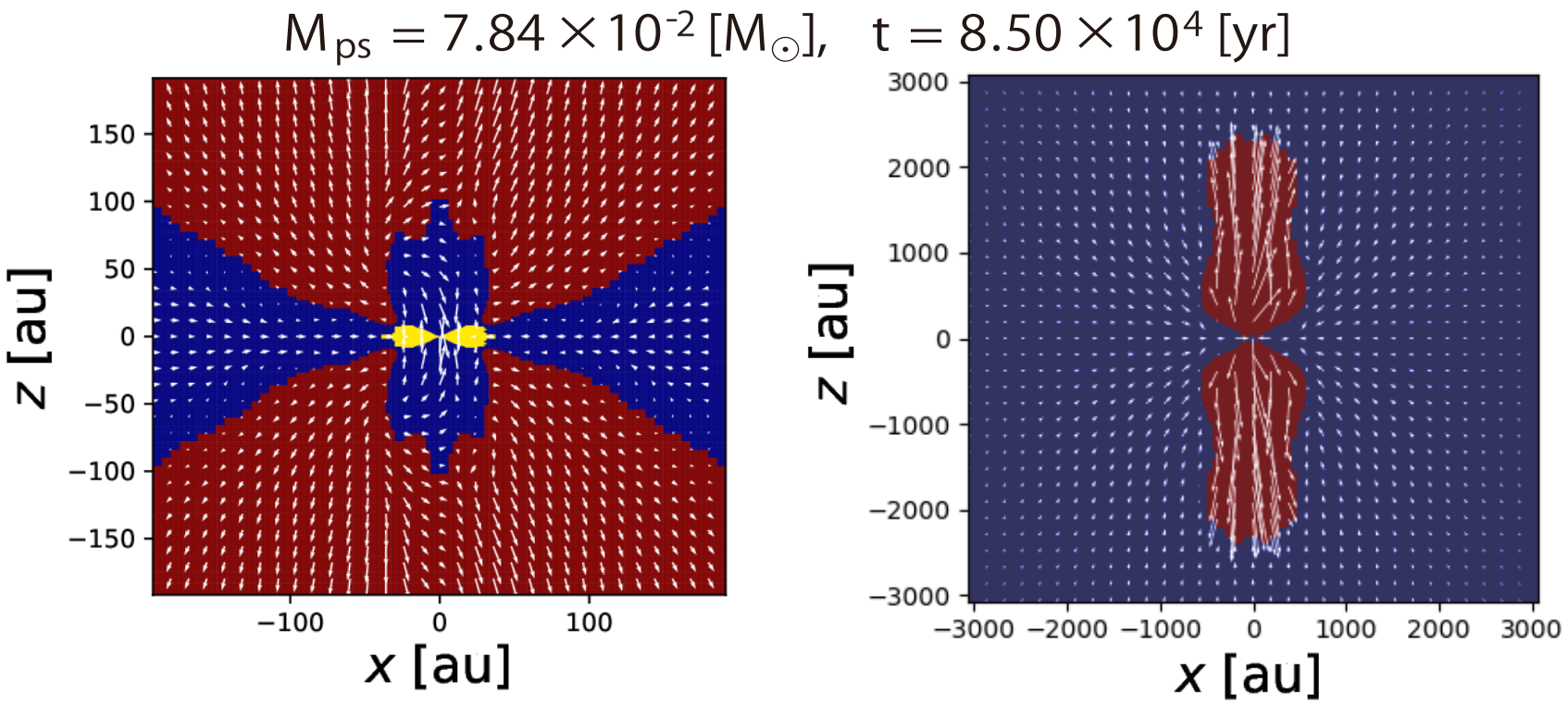

Figure 8: Four different regions, specifically, the envelope (deep blue), disk (yellow), outflow (red), and protostar, as classified by my criteria, in which the protostar region is not visible due to its small size compared to the scale of the panels. The arrows at each point indicate the velocity. The entire disk region is covered in the left panel, while the entire outflow region is plotted in the right panel. The protostellar mass (or sink mass) $M_{\rm ps}$ and the elapsed time *time* after the cloud begins to collapse are described in the upper part of each panel.

Next, the process used to assign weight to the mass with dust and gas particles based on the assumption that the weighted mass corresponds to the gas shell mass is explained. Note that the particles are uniformly placed in the initial cloud core, as described in §2.3.2. The gas mass of the shell dm_r, which is distributed on the radius r, is given by

$$dm_r = 4\pi\rho_r r^2 dr, \tag{25}$$

where ρ_r is the gas mass density at a radius r, and ρ_r is determined from the initial gas cloud described in §2.3.1. Adopting $dr = 1\,\mathrm{au}$, the radial direction is discretized according to the radial coordinates listed in Table 1. Then, each shell mass is normalized by the mass of the outermost shell, which is located at $r = 6130$ au. The shell mass ratio N is given by

$$N = \frac{dm_r}{dm_{6130\,\mathrm{au}}}. \tag{26}$$

To estimate f_{dg}, the shell mass ratio N is adopted for weighting all particles (six differently sized dust particles and one gas particle), which means that all particles have the internal parameter N. Fig. 7 plots the shell mass ratio N against the radius. To assign weight to the particle, I assume that each particle has the parameter of the 'mass ratio' N. Note that the weighting is the same as long as the initial position r is the same, even when the initial dust particle has different ϕ and θ.

In this study, I use the dust-to-gas mass ratio normalized by the initially and spatially uniform value of f_{dg} as δf_{dg} with each dust particle size a_{d}. The change in the dust-to-gas mass ratio δf_{dg} represents how much change f_{dg} from the initial value and is given by

$$\delta f_{\mathrm{dg}} = \frac{\sum_i N_{i,\mathrm{d}}}{\sum_i N_{i,\mathrm{g}}}, \tag{27}$$

where $N_{i,\mathrm{d}}$ and $N_{i,\mathrm{g}}$ are the mass shell ratio N of the $i-$th dust particle and the $i-$th gas particle, respectively, and the summation is only performed on the particles that satisfy the requirement described below.

Since it is difficult to estimate f_{dg} at each point with this method, instead of estimating f_{dg}, I calculate δf_{dg} for either the four distinct regions (envelope, protostar, disk, and outflow) or at various spatial scales. (For details, see §3.4.) In equation (27), the

summation is only executed for particles that fulfilled the conditions I imposed, which are described in detail in §3.4. It should be noted that an initially spatially uniform $f_{\rm dg}$ is not necessary for this study. However, since almost all similar studies have adopted $f_{\rm dg} = 0.01$ (e.g., Mathis et al. (1977) and Hayashi (1981)), I do not focus on the validly of $f_{\rm dg} = 0.01$ in this study. Instead, the time evolution of the change of $f_{\rm dg}$ is discussed from the initial value using $\delta f_{\rm dg}$.

2.5 Criteria characterizing each region

In this section, the computational domain within the star-forming core (or Bonnor-Ebert sphere) is classified into the four above-mentioned regions (envelope, protostar, disk, and outflow) based on the following criteria:

- Protostar: the region inside the sink cell, in which the sink radius is $r_{\rm sink} = 1$ au.
- Disk: the region where the gas rotational velocity is much faster than the radial velocity ($v_\phi > 2|v_r|$) and is supported by rotation to some extent ($v_\phi > 0.6\, v_{\rm K}$, where $v_{\rm K}$ is the Keplerian velocity).
- Outflow: the region where the radial velocity of the gas is faster than the speed of sound $c_{s,0}$ ($v_r > c_{s,0}$) defined in §2.1. [1]
- Envelope: the remainder of the computational domain within the star-forming cloud (or Bonnor-Ebert sphere).

The gas evolution in §3.1 and the time evolution of the dust-to-gas mass ratio in §3.4 are discussed based on these criteria, which were determined through trial and error while referring to Joos et al. (2012).

[1] I confirmed that the outflow region does not change significantly when a strict criterion (for example, $v_r > 2c_{s,0}$) is adopted.

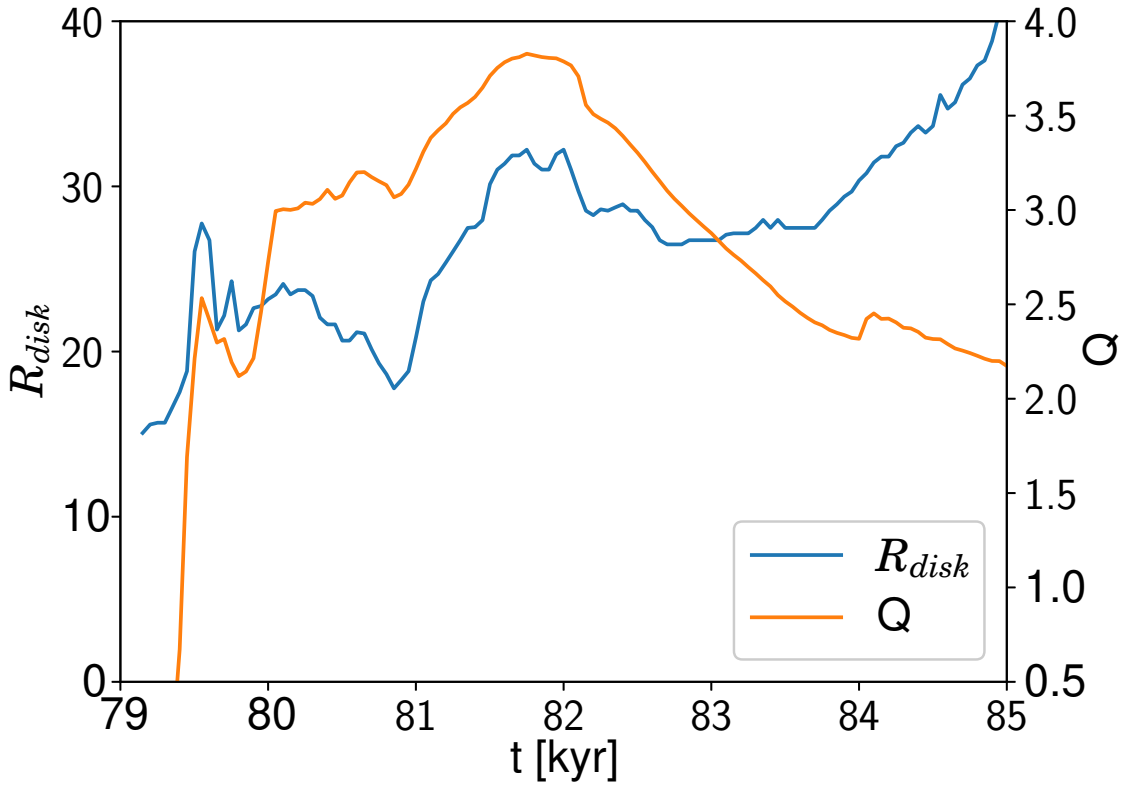

Figure 9: Time evolution of disk radius $R_{\rm disk}$ (blue, left axis) and Toomre's Q parameter (orange, right axis) against elapsed time.

3 Results

3.1 Gas fluid time evolution

The gas fluid time evolution is described in this subsection. Fig. 8 plots each region (disk, outflow, and envelope) determined using the criteria in §2.5 for different spatial scales. The entire disk region is covered in the left panel, and the entire outflow region is embedded in the right panel. As can be seen in the figure, the disk, outflow, and envelope regions are clearly divided by my criteria. The disk radius is about 40 au, and the outflow reaches about 3000 au at the end of the simulation. The outflow opening angle is about 60°.

Fig. 9 shows the time evolution of the disk radius $R_{\rm disk}$ and Toomre's Q parameter

(Toomre, 1964). The $R_{\rm disk}$ is determined as the distance from the center to the farthest cell, which fulfills the disk criteria on the equatorial plane. The Toomre's Q parameter is defined as

$$Q = \frac{\int_{\rho>\rho_{\rm crit}} \frac{c_s \kappa}{\pi G \Sigma} \Sigma dS}{\int_{\rho>\rho_{\rm crit}} \Sigma dS}, \tag{28}$$

where $\rho_{\rm crit}$ is the critical density, which is the minimum gas mass density in the disk region, c_s is the local sound speed, κ is the epicyclic frequency, G is the gravitational constant, and Σ is the gas surface density of the disk. I adopt $\kappa = \Omega_{\rm K}$ with $\Omega_{\rm K}$ defined as the local Keplerian frequency. The Q parameter described in equation (28) is the mass-weighted averaged value over the disk. As the study progressed, I confirmed that gas is continuously supplied from the envelope and that the disk is growing steadily. Note that, during the calculation, the disk becomes gravitationally unstable when the Q parameter becomes close to 1.

Fig. 10 plots the time evolution of the density and velocity distributions of the gas. The figure shows that a rotationally supported disk is formed at the center, and the disk gas is supplied from the envelope. In addition, I confirmed that the outflow is driven from the disk surface. This simulation was stopped at $t = 85000$ years after the cloud collapse begins, at which time the mass of the sink cell is $M_{\rm sink} = 0.0784 M_{\rm sun}$ and the disk has a radius of about 40 au. The next section discusses dust dynamics at this stage.

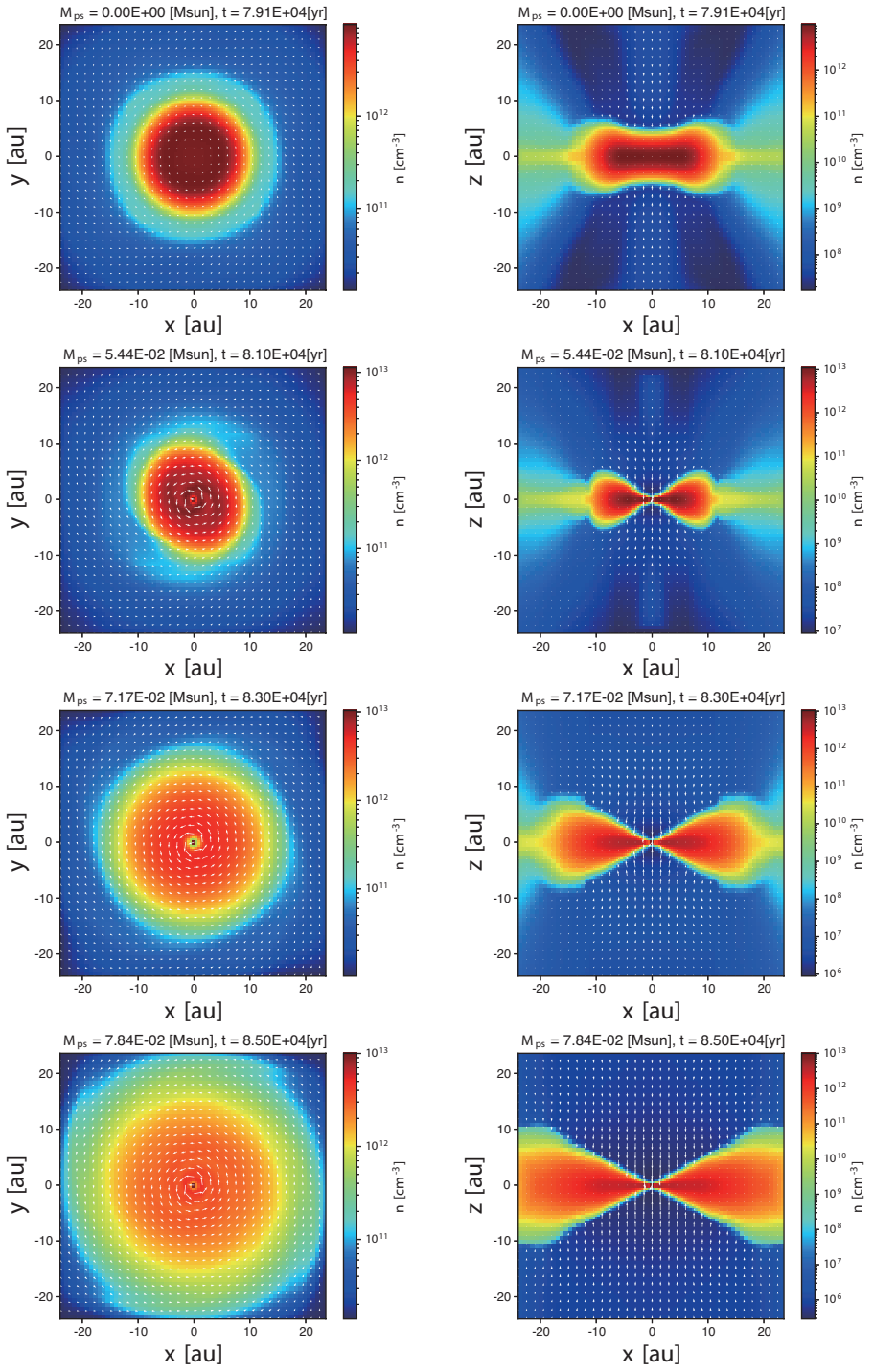

Figure 10: Time evolution of the gas number density (color) and velocity (arrows) on the $z = 0$ (left) and $y = 0$ (right) plane. The mass of the protostar (or sink particle) and the elapsed time are described in the upper part of each panel.

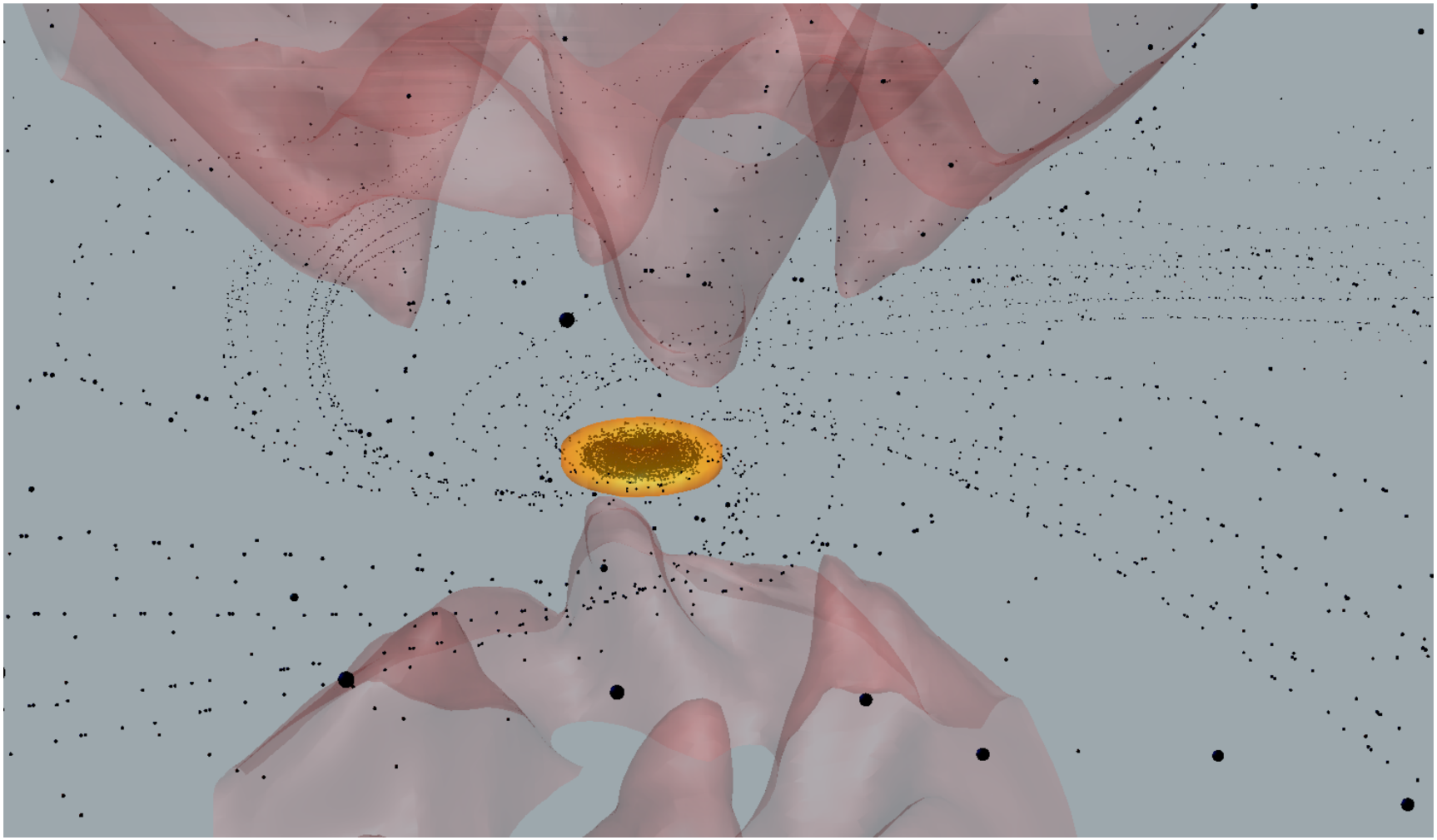

Figure 11: 3D structures of gas fluid and dust particles. The spatial scale is about 300 au. The yellow surface corresponds to the rotationally supported disk (surface iso-density of $n = 5 \times 10^{11}$ cm^{-3}), while the red surface indicates the outflow (surface iso-velocity of $v_r = 2$ km s^{-1}). The black points are dust particles (all sizes).

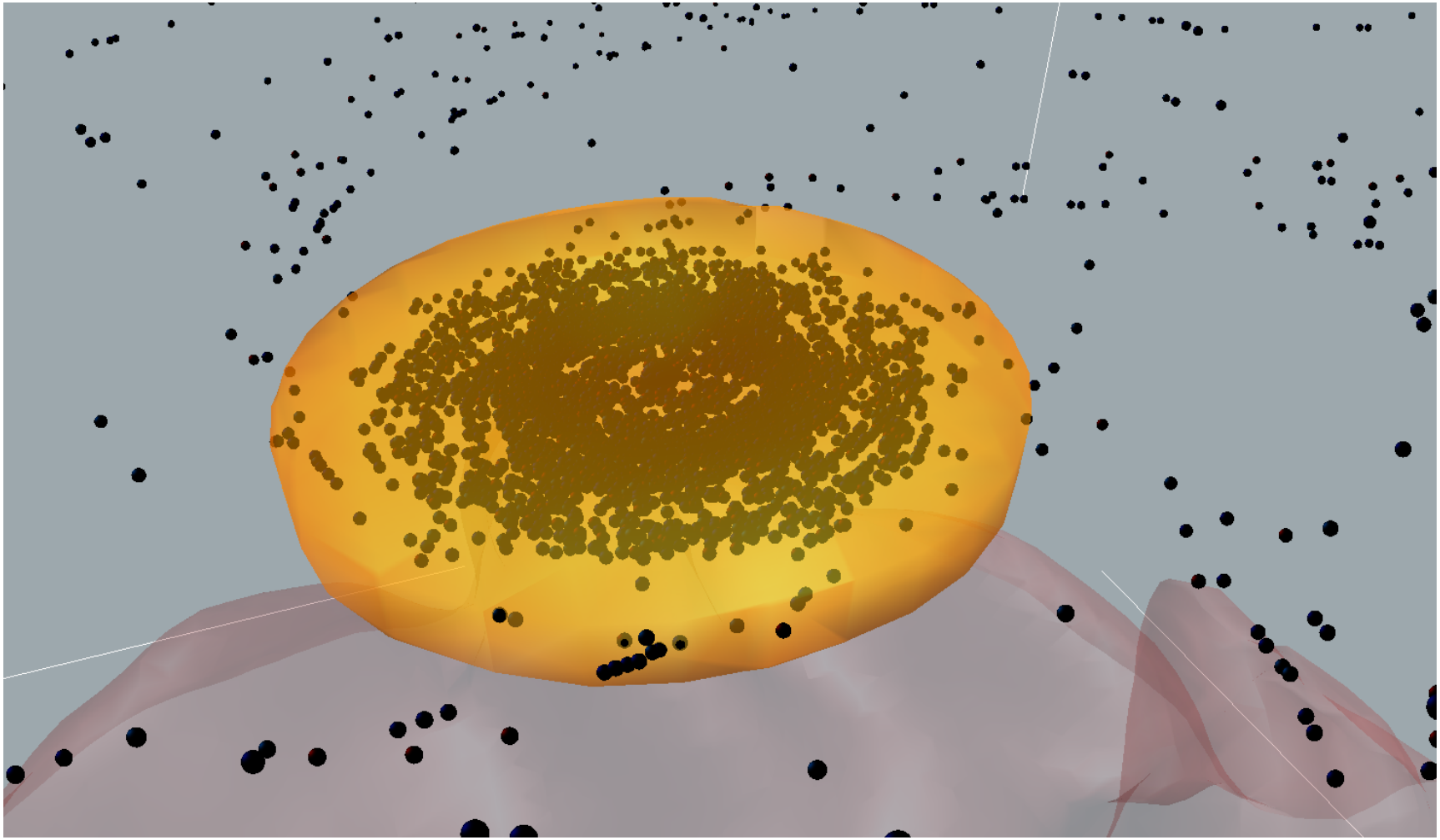

Figure 12: Same as in Fig. 11 but for a spatial scale of about 100 au.

3.2 Dust displacement

Figs. 11 and 12 show 3D spatial distributions of gas fluid and dust particles in which the yellow contour is the high-density or disk region ($n = 5 \times 10^{11}\mathrm{cm}^{-3}$) and the red contour corresponds to the outflow region ($v_r = 2\ \mathrm{km\,s}^{-1}$). Note that only the inner region of the rotationally supported disk, which has a minimum density of $\sim 10^{10}\,\mathrm{cm}^{-3}$, is represented by the yellow contour. In the figures, each black point corresponds to one of the dust particles that were initially distributed all over the initial cloud (or Bonnor-Ebert sphere). Fig. 11 covers about 300 au scale, while Fig. 12 is a close-up view of the area around the center. These figures indicate that numerous dust particles create a disk-like structure around the sink and that a portion of the dust particles is swept up by the gas outflow. The figures also indicate that the dust motion is almost the same as the gas fluid motion.

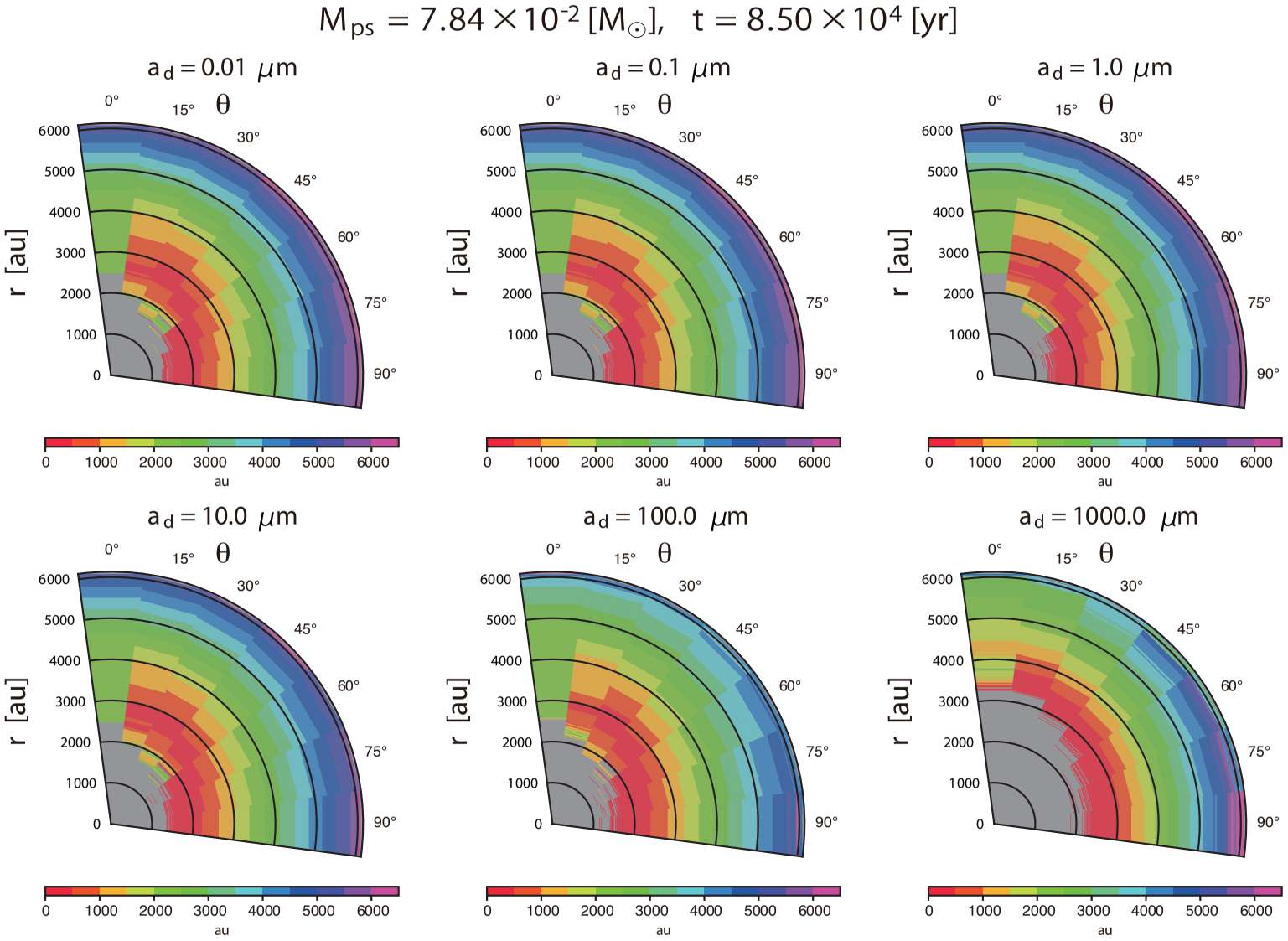

Figure 13: Distances of dust particles from the center at the end of the simulation (color) plotted on the initial r and θ position plane that was placed according to Table 1. The particles distributed in the gray region fall into the sink by the end of the simulation. The dust particle size $a_{\rm d}$, which is described in the upper part of each panel, differs in each panel.

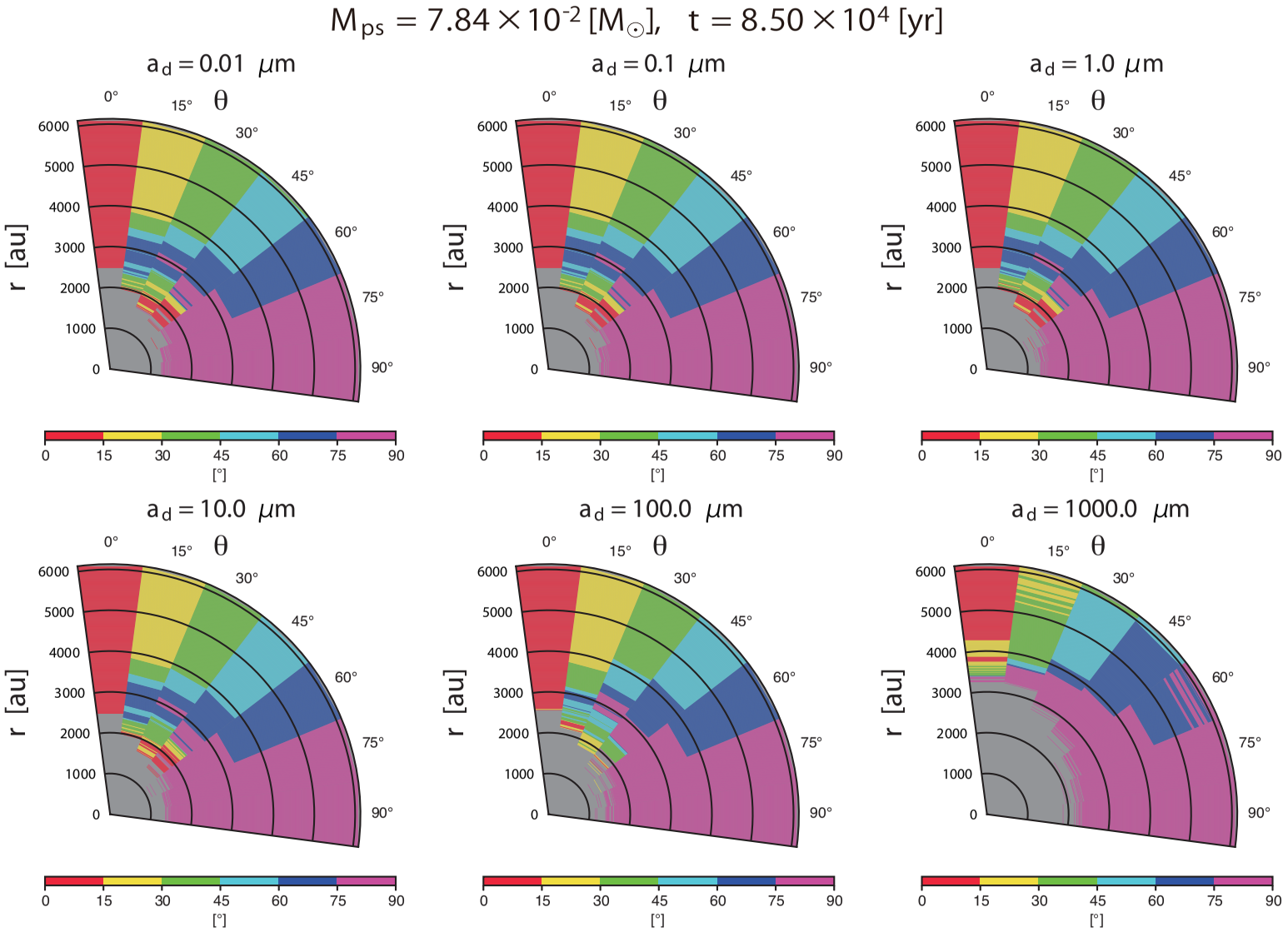

Figure 14: Same as Fig. 13 but the color indicates the zenith angle.

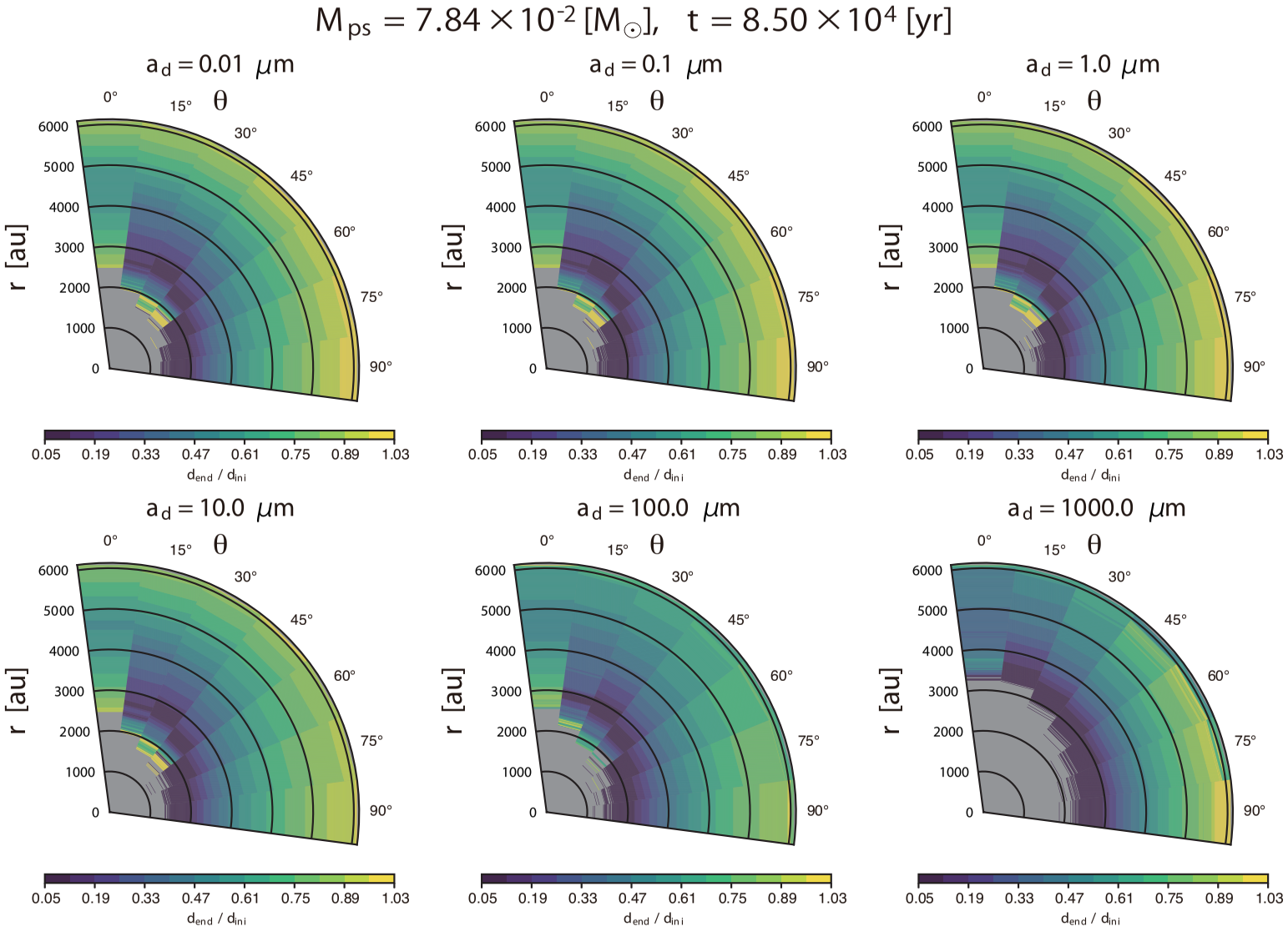

Figure 15: Same as in Fig. 13 but with colors indicating the dust particle distance ratios of the epochs during the period between the simulation end and the initial state.

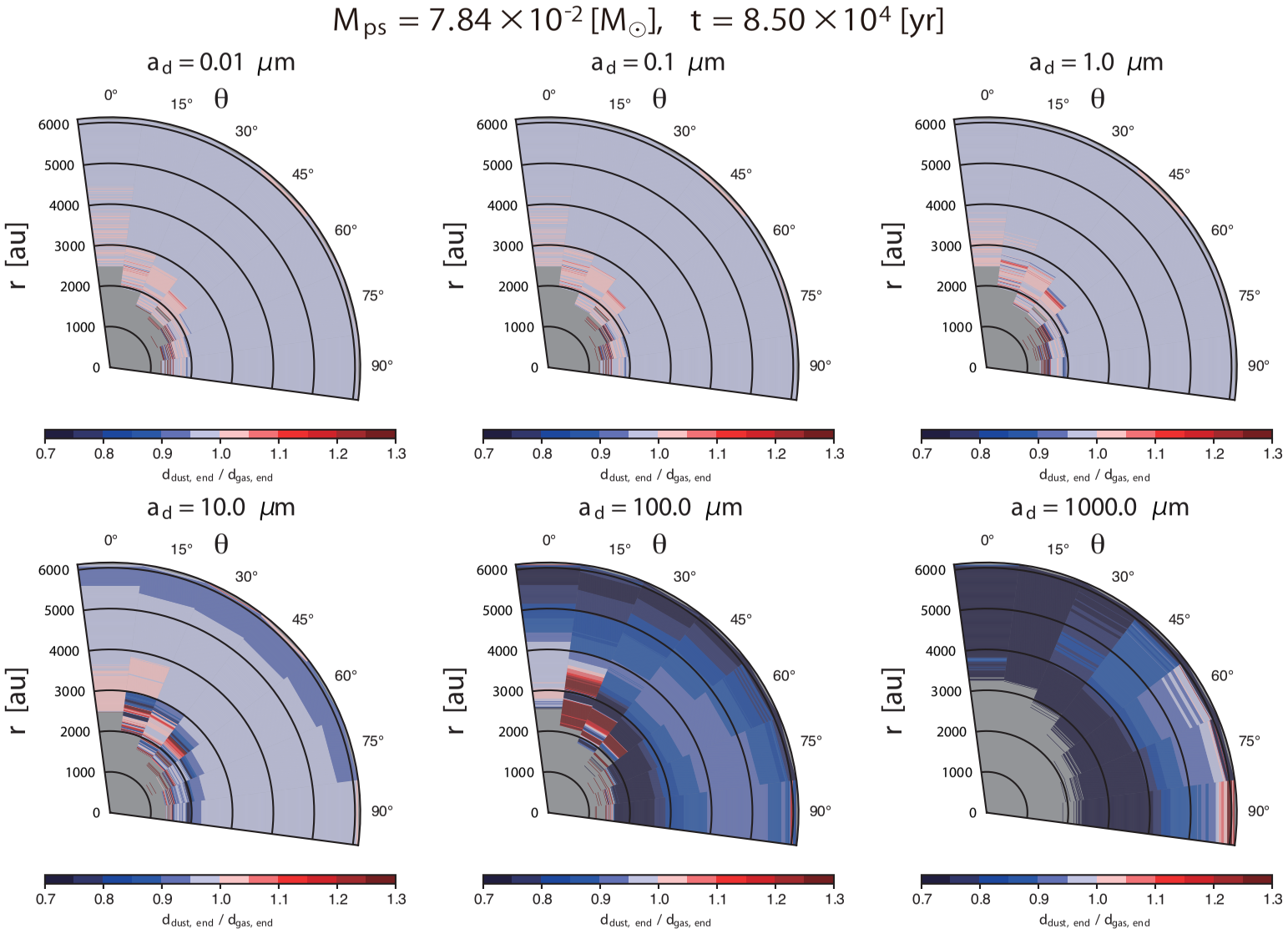

Figure 16: Same as in Fig. 13 but with colors indicating the dust particle distance ratios relative to the gas particles that were initially located at the same position ($d_{\mathrm{dust,end}}/d_{\mathrm{gas,end}}$).

Fig. 13 shows dust particle distances from the center at the end of the simulation. This figure consists of six panels, and each panel contains the result for a different dust particle size $a_{\rm d}$. Here, r and θ correspond to the initial and end positions, respectively, of each dust particle, while the color scale shown indicates the distance from the center at the simulation end.The particles in the gray area have already fallen into the sink. For simplicity, only particles with $\phi = 0°$ are plotted since I confirmed almost the same result in other cases of ϕ ($\phi = 90, 180, 270°$). My simulations showed that the dust particles initially located at large θ, which have large specific angular momentum values, tend to fall into the center later.

At the simulation end, the dust particles initially distributed in the $\theta \simeq 0°$ direction with sizes of $0.01\,\mu{\rm m} \leq a_{\rm d} \leq 100\,\mu{\rm m}$ have been collected for $r > 2000\,{\rm au}$ by the gas outflow, except for the particles that have already fallen into the sink. In contrast, the large particles ($a_{\rm d} = 1000\,\mu{\rm m}$, Fig.13 bottom right) show different behavior than relatively small particles and, overall, dust particles with $a_{\rm d} = 1000\,\mu{\rm m}$ tend to rapidly fall into the center due to their longer stopping times (§3.5).

Fig. 14 shows the zenith angle for dust particles $\theta_{\rm end}$ at the end of the calculation plotted on the initial r and θ location planes. Here, it can be seen that some dust particles with $15° \leq \theta \leq 75°$ tend to have a larger zenith angle $\theta_{\rm end}$ than their initial angle. This tendency is stronger for particles located relatively close to the center. In addition to gravity, gas motion is also governed by the Lorentz force, and the magnetic field lines have an hourglass shape. Thus, the dust particles coupled with gas move along magnetic field lines and reach the region with a large zenith angle (the purple region in Fig. 14). Almost all the dust particles initially distributed around the z-axis (or particles with $\theta = 0°$) maintain their initial zenith angle, while the trajectories of some of the particles with $a_{\rm d} = 1000\,\mu{\rm m}$ are disrupted by the outflow. In addition, the figure indicates that the dust particles initially distributed near the equatorial plane are not swept up by the outflow.

Fig. 15 shows the dust particle distance ratios during the period between the simulation end and the initial state ($d_{\rm end}/d_{\rm ini}$, where $d_{\rm end}$ and $d_{\rm ini}$ are the particle distances from the center at the simulation end and the initial state, respectively). In the figure, the colors indicate how close a particle is to the center of the gravitationally collapsing cloud. This figure indicates that the particles initially placed around the center ($r \lesssim 2000\,{\rm au}$) tend to rapidly fall into the sink or protostar. In contrast, the dust particles swept up by the outflow

first approach the central region and then move to the outer region. Thus, the ratios for such particles are larger than those for other particles shown in Fig. 15. For example, in the case of $a_{\rm d} = 0.01\ \mu$m, the particles initially placed within the range of $r \sim 4000-5000$ au along the z-axis (i.e., $\theta = 0$) have lower ratios than other particles located at the same angle. This is because the dust particles initially located around the $z-$axis move with the gas outflow within $r \lesssim 4000$ au. In addition, the particles outside of 5000 au slowly approach the center along the $z-$axis because the outflow interrupts their rapid fall, and none of the particles have distance ratios that exceed unity (i.e., $d_{\rm end}/d_{\rm ini} < 1$), thus indicating that no particles move outward from their initial positions within the simulation time. However, with further time integration, it is expected that the ratio ($d_{\rm end}/d_{\rm ini}$) exceeds unity, and the dust particles are ejected from the collapsing cloud core.

Fig. 16 shows the ratio of the distances of the dust particles to those of the gas particles at the end of the calculation ($d_{\rm dust,end}/d_{\rm gas,end}$). Since I estimated the ratios for each of the dust and gas particles that were located at the same initial position, this figure indicates how far each dust particle had separated from its associated gas particle at the end of the simulation. The dust particles are well coupled with the gas when the ratios are almost unity but are decoupled when the ratios are not unity. This figure also shows that dust particles $0.01\ \mu{\rm m} \leq a_{\rm d} \leq 10\ \mu$m in size are broadly coupled with the gas. In contrast, in the case of $a_{\rm d} = 1000\ \mu$m, in which the distance from the center is smaller for the dust particles than for the gas, the dust particles are decoupled, thus indicating that the dust particles are more concentrated towards the center than is the gas. Dust particles with sizes of $a_{\rm d} = 100\ \mu$m are also noticeably decoupled from the gas. Interestingly, for the case of $a_{\rm d} = 100\ \mu$m, some dust particles that were distributed in the range of $2000\ {\rm au} \leq r \leq 3000\ {\rm au}$ with $15^\circ \leq \theta \leq 45^\circ$ are more distant from the center than the gas. This occurred because those particles reached the gas outflow driving area earlier than the gas particles that shared their same initial positions.

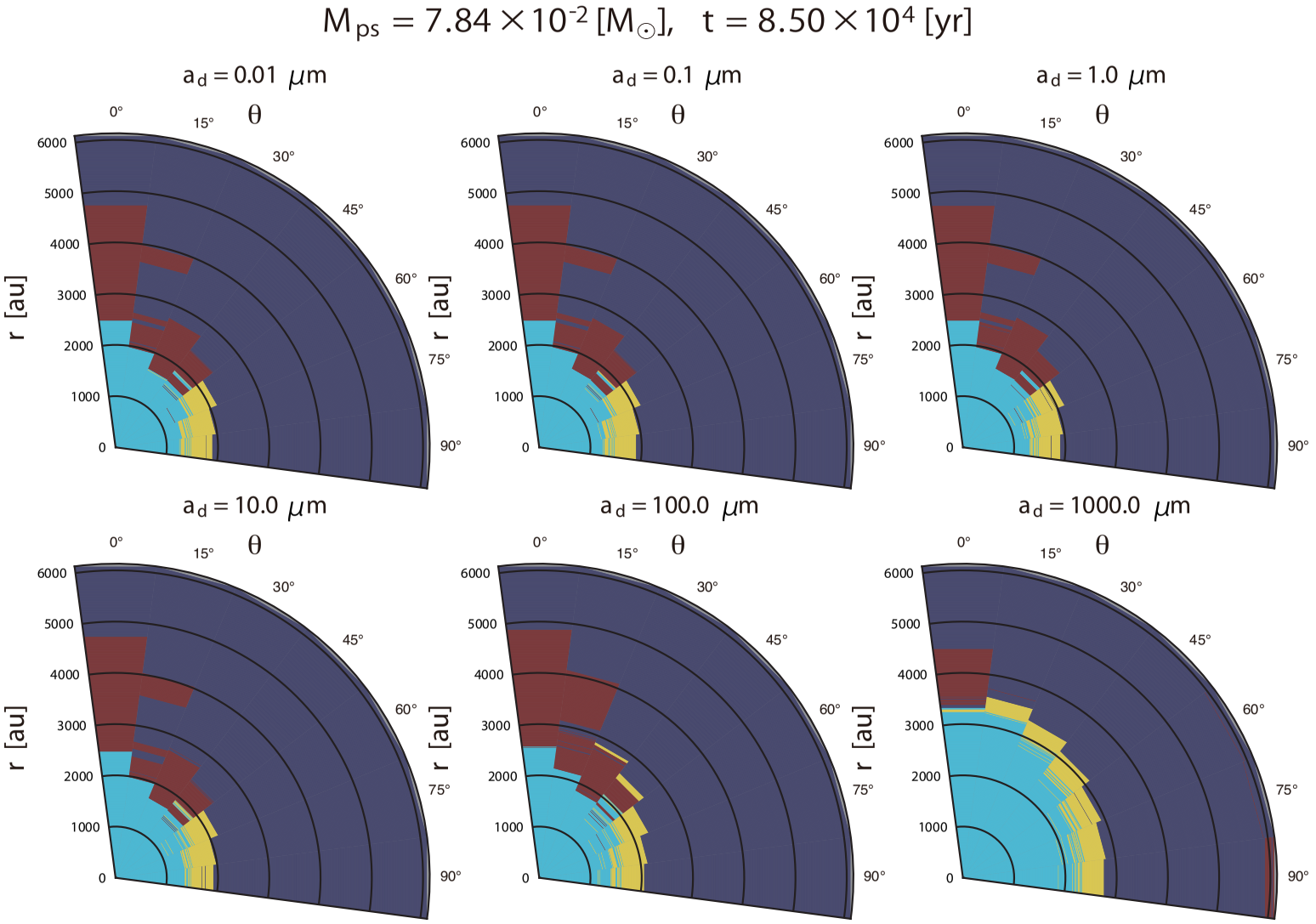

Figure 17: Same as in Fig. 13 but with colors indicating the envelope (deep blue), protostar (light blue), disk (yellow), and outflow (red).

3.3 Dust initial position and gas regions

Since dust particles are introduced as particles in this study, it is possible to trace their motion. In §3.1, the computational domain is classified into four different regions (envelope, protostar, disk, and outflow) based on some physical criteria. In this subsection, I specify the regions to which the dust particles belong in terms of the initial position plane (r, θ) and dust size ($a_{\rm d}$). Fig. 17 shows the associated region of the dust (color) on the initial position (r, ϕ) plane, on which the envelope (deep blue), protostar (light blue), disk (yellow) and outflow (red) regions are plotted. I begin by focusing on particles belonging to the outflow (red) region. The dust particles placed within the outflow only come from $0^\circ \leq \theta \leq 45^\circ$ when their sizes are within the range of 0.01 μm $\leq a_{\rm d} \leq$ 100 μm. In the figure, dust particles $a_{\rm d} = 100\,\mu$m in size have a wider outflow region than dust particles with sizes of $a_{\rm d} < 100\,\mu$m ($a_{\rm d} = 0.01.$ 0.1, 1.0, 10 μm), thus indicating that dust particles $a_{\rm d} = 100\,\mu$m in size are preferentially ejected by the outflow. In contrast, dust particles $a_{\rm d} = 1000\,\mu$m in size are only swept up by the outflow when they are initially placed along the $z-$axis with $\theta = 0^\circ$.

Next, the particles within the disk are examined. When the dust particle size satisfies $a_{\rm d} \leq 100\,\mu$m, only those particles initially located in the range of $60^\circ \leq \theta \leq 90^\circ$ can enter the disk and rotate with the gas. In contrast, particles with a size of $a_{\rm d} = 1000\,\mu$m reach the disk with a wide range of θ ($15^\circ \leq \theta \leq 90^\circ$).

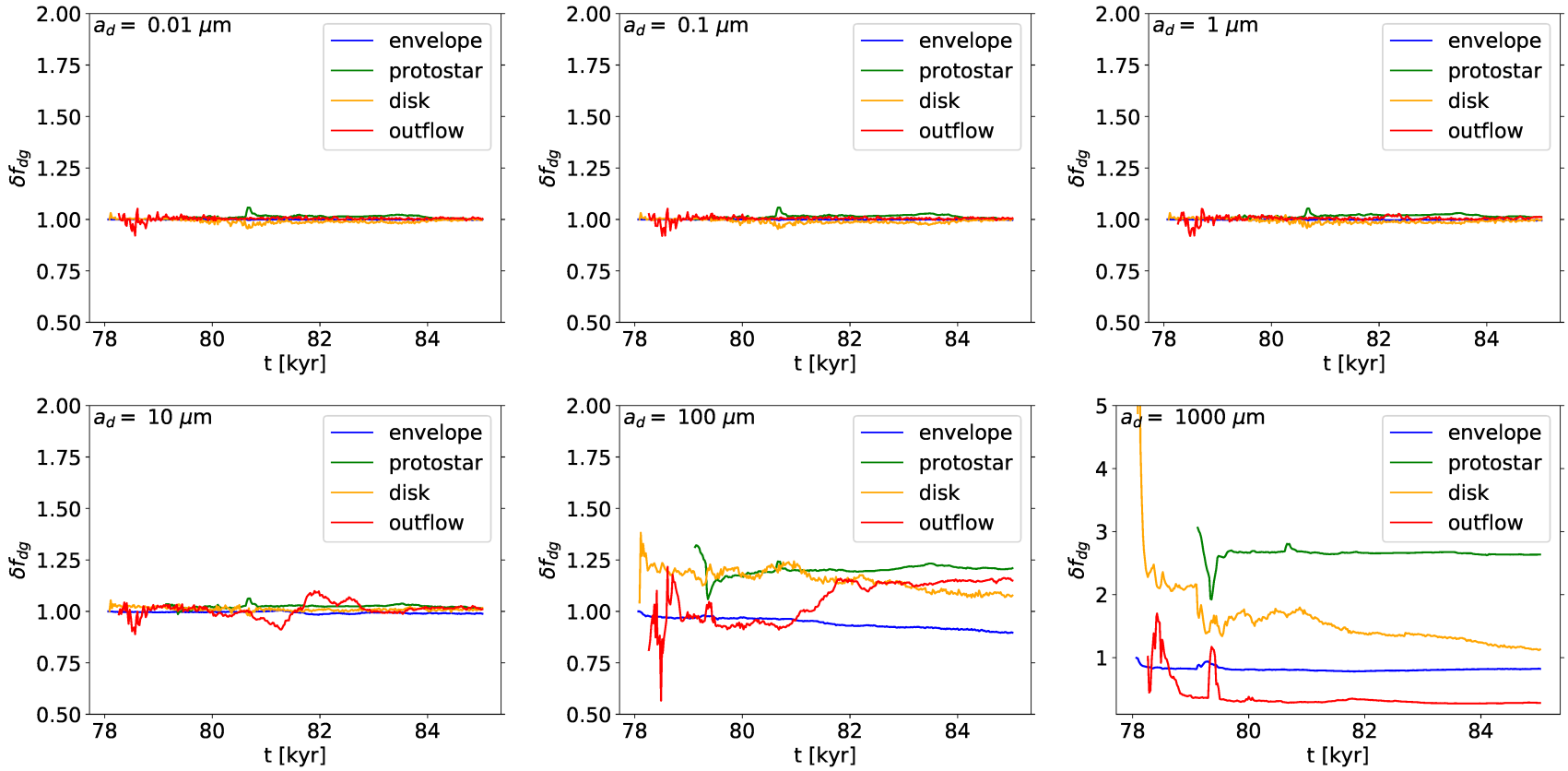

Figure 18: Time evolution of changes to the dust-to-gas mass ratio $\delta f_{\rm dg}$ with different dust sizes ($a_{\rm d}$ = 0.01-1000 μm). In each panel, dust particles belonging to the four different regions of envelope (blue), protostar (green), disk (yellow), and outflow (red) are presented.

3.4 Dust-to-gas mass ratio

Figs. 18, 19 and 20 show the time evolution of changes to the dust-to-gas mass ratio $\delta f_{\rm dg}$ that is defined in §2.4. Fig. 18 plots $\delta f_{\rm dg}$ belonging to the envelope, protostar, disk, and outflow regions (for definitions, see §3.1). For dust particles 0.01 μm $\leq a_{\rm d} \leq$ 10 μm in size, the $\delta f_{\rm dg}$ is within the range of 0.9 to 1.1. Thus, at most, $f_{\rm dg}$ changes within 10 % from the initial positions. When dust particles are $a_{\rm d} \geq 100$ μm in size, a noticeable difference can be seen from the size of $a_{\rm d} \leq 10$ μm in the $f_{\rm dg}$ time evolution.

Because they are disturbed by the outflow, dust particles with $a_{\rm d} = 100$ μm are concentrated in not only the relatively high-density region (protostar and disk) but also in the low-density region (outflow). A concentration of larger dust particles in a high-density region was also reported in Lebreuilly et al. (2020). Conversely, the $\delta f_{\rm dg}$ with a size of $a_{\rm d} = 100$ μm decreases to $f_{\rm dg} = 0.8$ in the envelope region at the end of the simulation. The bottom right panel of Fig. 18 indicates that dust particles $a_{\rm d} = 1000$ μm in size tend to fall rapidly and behave considerably differently than dust particles $a_{\rm d} = 100$ μm in size seen in the outflow region. The dust particles that are $a_{\rm d} = 1000$ μm in size are expelled from the low-density gas region (envelope and outflow) because they have been decoupled from the lower density gas. This picture agrees well with Lebreuilly et al. (2020). For dust particles $a_{\rm d} = 1000$ μm in size, $\delta f_{\rm dg}$ in the outflow region decreases to 0.3, while that in the protostar region increases to 3.0.

Figs. 19 and 20 plot $\delta f_{\rm dg}$ with a different spatial scale in which I estimated the dust-to-gas mass ratio change within a sphere with a radius R. These figures indicate that the time evolution of the spatial distribution of $\delta f_{\rm dg}$ strongly depends on the dust particle size. As shown in Fig. 18, the dust particles that are 0.01 μm $\leq a_{\rm d} \leq$ 10 μm in size are coupled with gas due to their short stopping times. Particles with sizes larger than 100 μm fall into the center significantly faster than the gas, which is exaggerated on smaller scales. Thus, over the short term, large-sized dust particles should tend to be more concentrated in the center. Dust particles 100 μm in size behave differently from those with 100 μm because they are effectively swept up by the gas outflow.

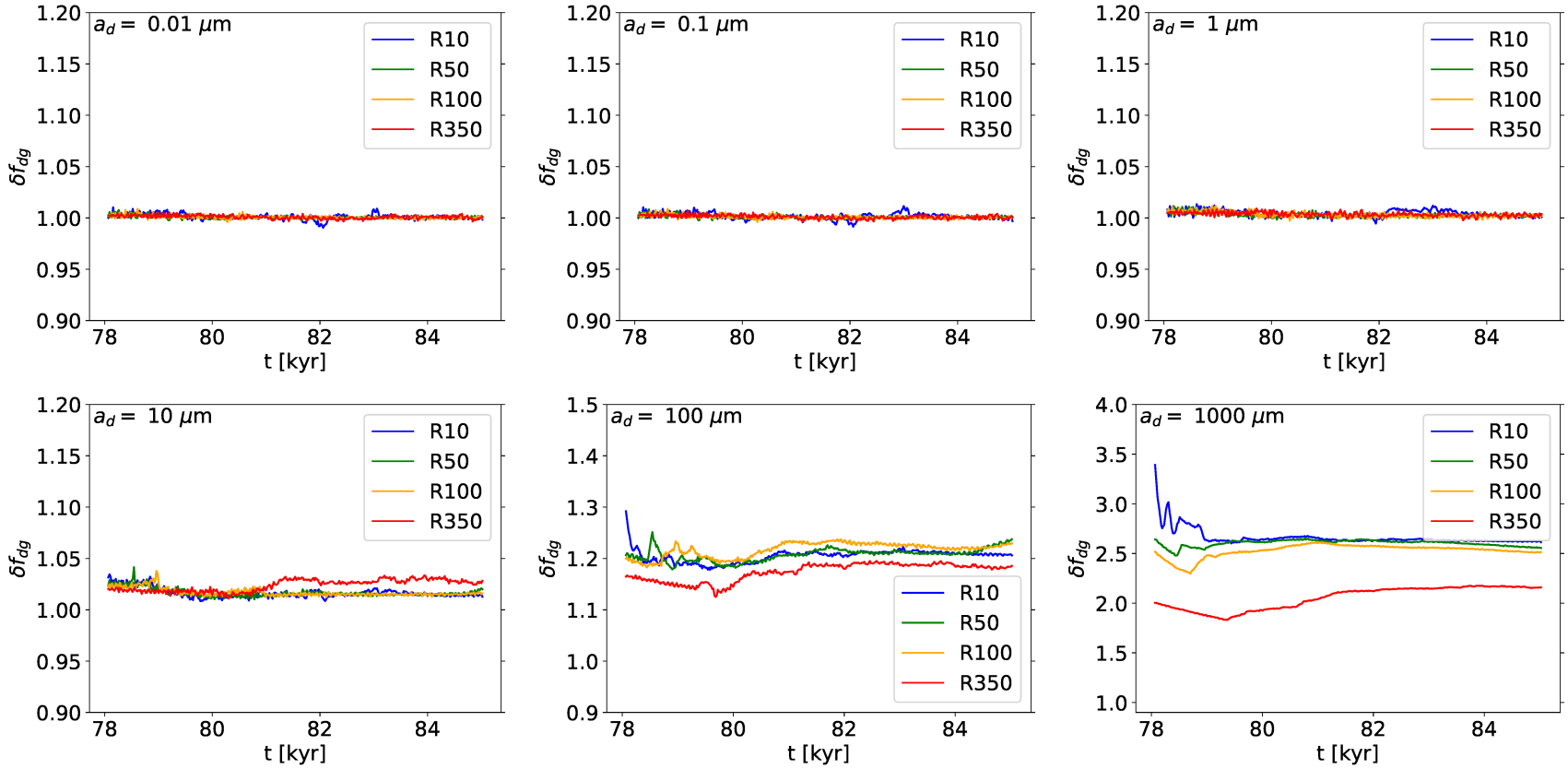

Figure 19: Same as in Fig. 18 but the colors in each panel indicate the scales: the sphere within 10 (blue), 50 (green), 100 (yellow), and 350 (red) au.

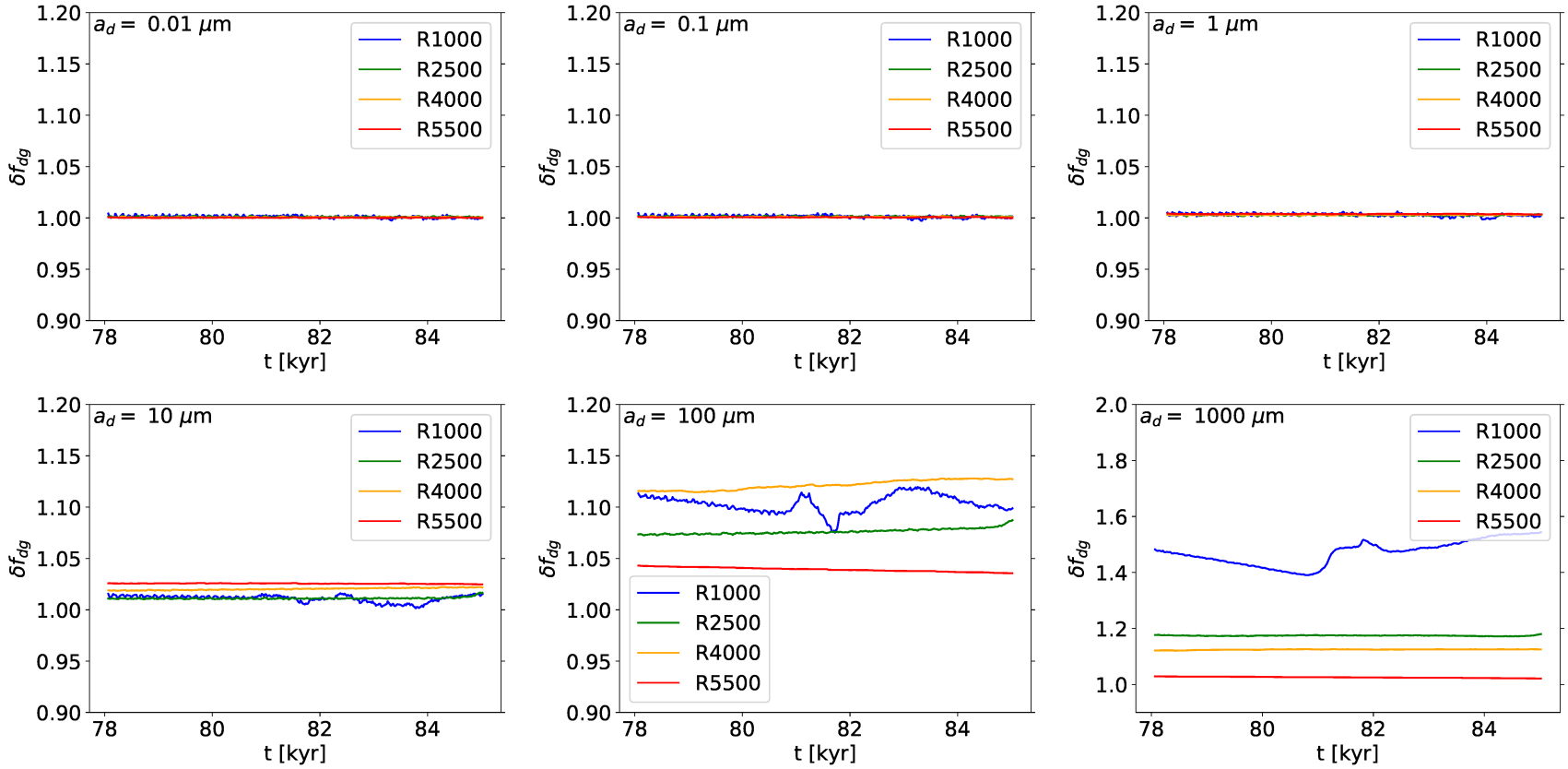

Figure 20: Same as in Fig. 18 but the colors in each panel indicate the scales: 1000 (blue), 2500 (green), 4000 (yellow), and 5500 (red) au.

3.5 Stokes number

In this section, I discuss how the dust particles are coupled with gas during the numerical simulation. To evaluate the coupling strength, the Stokes number defined in §2.3.2 is used. Fig. 21 shows the St for each dust particle at each position. The large particles tend to have large St values because their stopping time t_s is proportional to the particle size (see eq. (9)). In the figure, the St values for dust particles that are $0.01\,\mu\mathrm{m} \leq a_\mathrm{d} \leq 10\,\mu\mathrm{m}$ in size are always below unity (i.e., St < 1). Thus, these particles are coupled with the gas. Conversely, a portion of the dust particles that are $a_\mathrm{d} \geq 100\,\mu\mathrm{m}$ in size exceed unity (i.e., St > 1). The St increases in the low gas density region because the stopping time t_s becomes longer. In other words, the momentum exchange between the dust particles and gas molecules becomes inefficient in such a region. This can be confirmed in equation (9), in which the stopping time t_s is inversely proportional to the gas density.

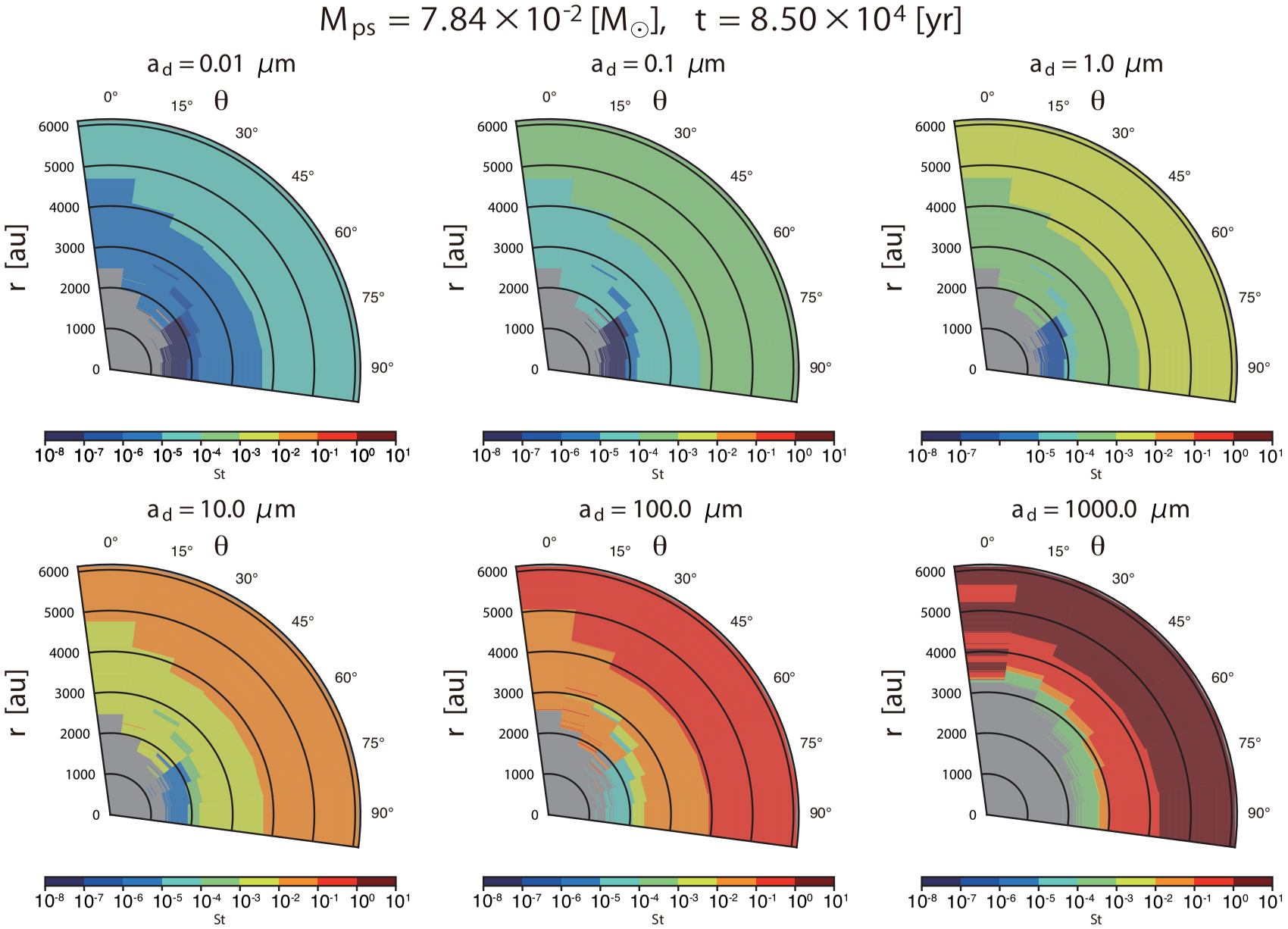

Figure 21: Same as in Fig. 13 but the color in each panel refers to the Stokes number St ($\equiv t_s/t_{ff}$) for the dust particle at each position.

Fig. 22 shows the St time evolution for several selected particles placed at different initial positions. In each panel, St decreases when the dust particle is located in a high gas density region such as the disk. The dust particles $0.01\,\mu\mathrm{m} \leq a_\mathrm{d} \leq 10\,\mu\mathrm{m}$ in size move in a gas envelope with a relatively large St. In contrast, when the dust particles move into the disk where the density is high, St decreases significantly. For example, at 79.5 kyr for $a_\mathrm{d} = 0.01\,\mu$m is initially located at $r = 3000$ au (green) and $\theta = 0°$(solid). However, as seen in each panel, St for these particles never reaches unity. Thus, these particles remained coupled with the gas during the simulation.

The dust particles $a_\mathrm{d} \geq 100\,\mu$m in size have $St \sim 1$ in the envelope. Thus, these particles fall into the central region faster than the gas because they are (partially) decoupled from the gas fluid. Therefore, the dust-to-gas mass ratio can significantly change in the envelope, as shown in Figs. 18, 19, and 20. However, St for these particles significantly decreases as they approach the disk center. As seen in Fig. 22, even for those dust particles, $\mathrm{St} \lesssim 10^{-3}$ within $r \lesssim 1000 - 2000$ au inside the region in which the disk is embedded. Thus, even though dust particles $a_\mathrm{d} \geq 100\,\mu$m in size fall rapidly into the disk, they are coupled with the gas and move together with the rotating fluid inside the disk.

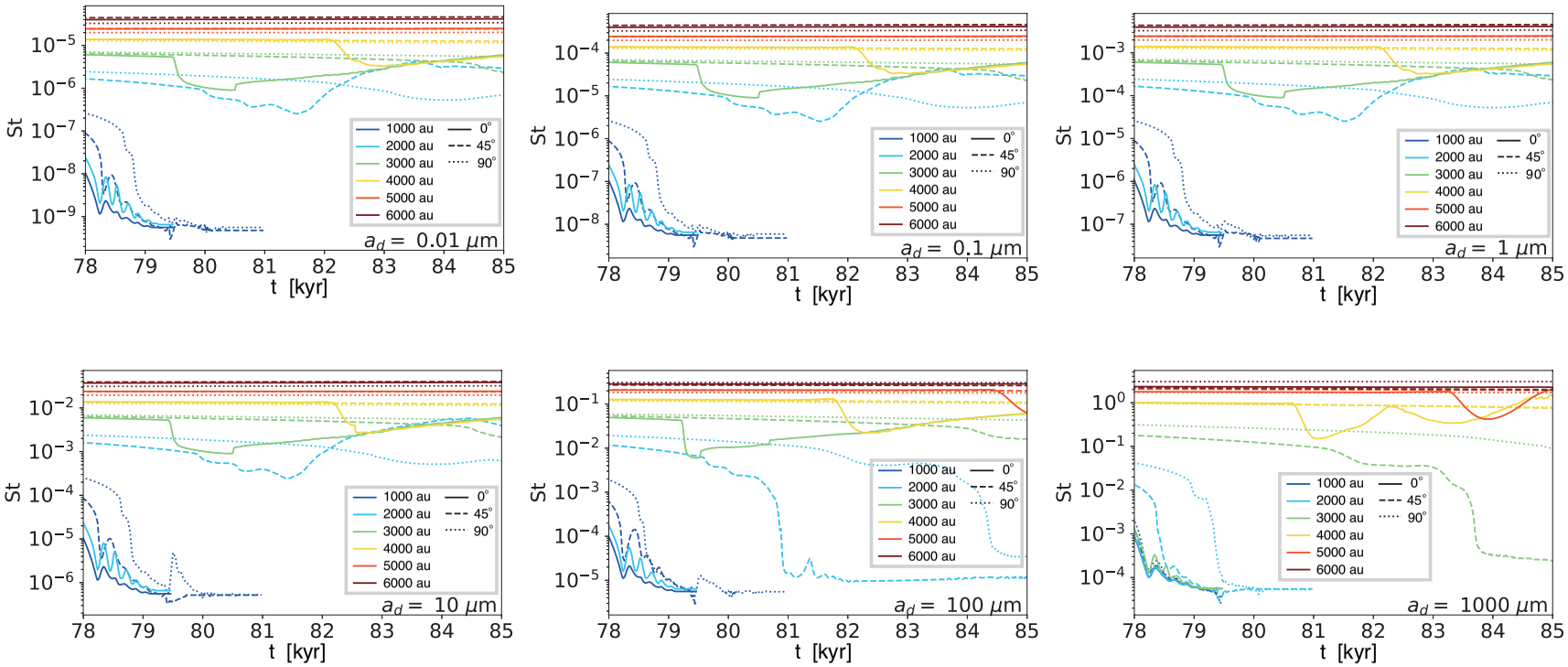

Figure 22: Stokes number St for selected particles placed at different initial positions against the elapsed time. In each panel, the dust particle size $a_{\rm d}$ that is described in the bottom right corner is the same. The initial distance from the center of each particle is presented by the color and the initial angle θ is presented by different line styles. The line breaks when the particle falls into the sink before the simulation ends.

3.6 Dust particle trajectories

Since dust particles were introduced into the numerical simulation as super-particles, the trajectory of each particle with gas evolution could be traced. In this subsection, the results for particle trajectories are provided based on their initial positions. Fig. 23 and Fig. 24 shown the time evolution of the radial distances from the center of the dust particles with sizes of 0.01μm and 1000μm, respectively. Hereafter, the distances are defined in two dimensions as $r = \sqrt{x^2 + y^2}$. Each group of figures presents the results for the initial zenith angle $\theta = 0, 15, 30, 45, 60, 75, and 90^\circ$ for the dust particles in the order of the top row left, right; the second row left, right; and so on. First, the results plotted in Fig. 23 ($a_{\rm d} = 0.01\mu$m) are discussed. The dust particles shown in Fig. 23 that have $r = 1000 - 2450$ au are initially chosen, and in the following explanation, only those particles that satisfy this condition are considered. Dust particles that initially satisfy $\theta = 0^\circ$ have already penetrated the sink particle by $t = 80$ kyr. These particles fall due to the gravity of the central star even though the gas pressure gradient retards their decline to some extent. Furthermore, they are not swept up by the outflow because they fall before the outflow begins. Dust particles with $\theta = 15^\circ - 45^\circ$ located relatively near the center follow a ballistic trajectory as they fall into the central star. In contrast, dust particles that are relatively far from the center are gathered up by the gas outflow and follow its rotation as they move away from the center. Of course, such dust particles are pulled in the direction of the central star by gravity before being captured by the outflow. In the panels for dust particles with $\theta = 30^\circ, 45^\circ$, it can be seen that some of the particles initially fall into the central region of the gas envelope where r decreases, after which they are entrained by the gas outflow, and r begins to rise.

Next, particles moving into the disk are discussed. I begin by examining a particle with $\theta = 30^\circ$ and $r = 1650$ au, which is moving while maintaining a distance of 10 au from the center. This dust particle does not immediately fall to the equatorial plane of the disk but instead takes 10 rotations at $z \sim 3$ au before reaching the equatorial plane. Accordingly, it is considered to be rotating in the hydrostatic equilibrium region of the gas disk. However, particles with $\theta = 45^\circ$ and $r = 1850, 1900$au continue to fall into the center while dust particles located before and after them are rolled up by the outflow. This is because the

outflow launching point is oscillating, and the timing of the dust particles reaching the disk surface influences whether or not they are swept up into the outflow. Dust particles at $\theta = 60° - 90°$, which are initially closer to the equatorial plane, are not swept up in the outflow. They enter the disk and rotate instead. Interestingly, dust particles that enter the disk after the central star and disk have evolved to some extent do not fall into the central star but instead rotate while maintaining $r = 10$ au.

Fig.24 shows the time evolution of r for a dust particle with a size of 1000 μm. Here, it is important to note that the initial distances of the particles from the center are different from Fig.23. Basically, as with the dust at 0.01 μm, there are dust particles that become captured by gas outflow, rotate in the disk, and then fall into the central star. However, a larger fraction of the dust particles accrete and rotate in the disk than the 0.01 μm dust particles because dust particles with sizes of 1000μm are initially more decoupled from the gas than the dust particles with sizes of 0.01μm. As a result, they congregate faster in the central region where the disk is formed. The initial θ for the dust described above, which rotates at 10 au, has a wider range, $15° - 90°$. These "non-falling" dust particles are closely related to the radial drift barrier problem, which is one of the most important issues that have been discussed in relation to theoretical planet formation models for many years. Hereafter, I will focus on the trajectories of such particles.

Fig.25 shows the trajectory of the selected dust particle with a size of 0.01 μm, which it is initially located at $\theta = 90°, r = 1500$ au. The plotted dust particle rotates 30 times without falling by the end of the calculation. The dust particles initially located at the equatorial plane ($\theta = 90°$) and entering the disk after the formation of the rotating disk do not fall into the central star with a spiral structure. Instead, they rotate at 10 au.

Next, the trajectory of a dust particle that falls onto the central star is shown. Fig.26 shows the trajectory of a particle with initial positions of $r = 1900$ au, $\theta = 45°$, and $a_{\rm d} = 0.01$ μm. This particle falls into the equatorial plane of the disk while decreasing its distance $r = \sqrt{x^2 + y^2}$ from the center. After reaching the equatorial plane, the particle falls to the central star by following a spiral orbit for about 4000 years instead of adopting a circular motion with a radius of 10 au. This behavior is unlike that of the particle plotted in Fig. 25. Among the dust particles with $\theta = 45° - 75°$, particles that accrete into the equatorial plane of the disk and then spiral into the sink particle can be considered to satisfy the condition that they begin falling to the equatorial plane at a distance of less than

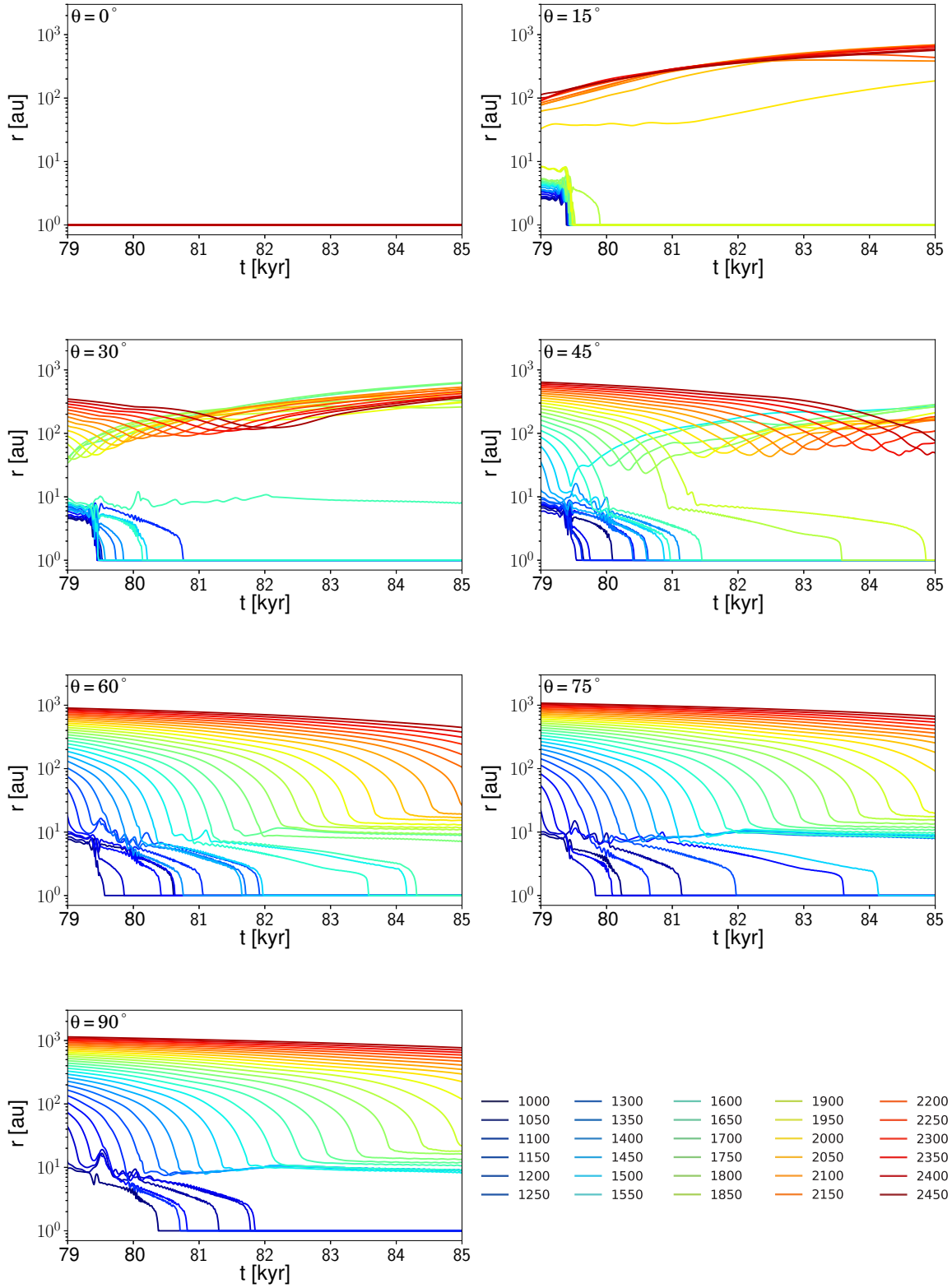

Figure 23: 2D time evolution of dust particle distances from the center. Each panel shows the results for $\theta = 0, 15, 30, 45, 60, 75, and 90°$ (from left top to right bottom). The dust particle size is $a_{\rm d} = 0.01$ μm. The numbers plotted in the right bottom are the colors corresponding to the initial distances ([au]) of the particles.

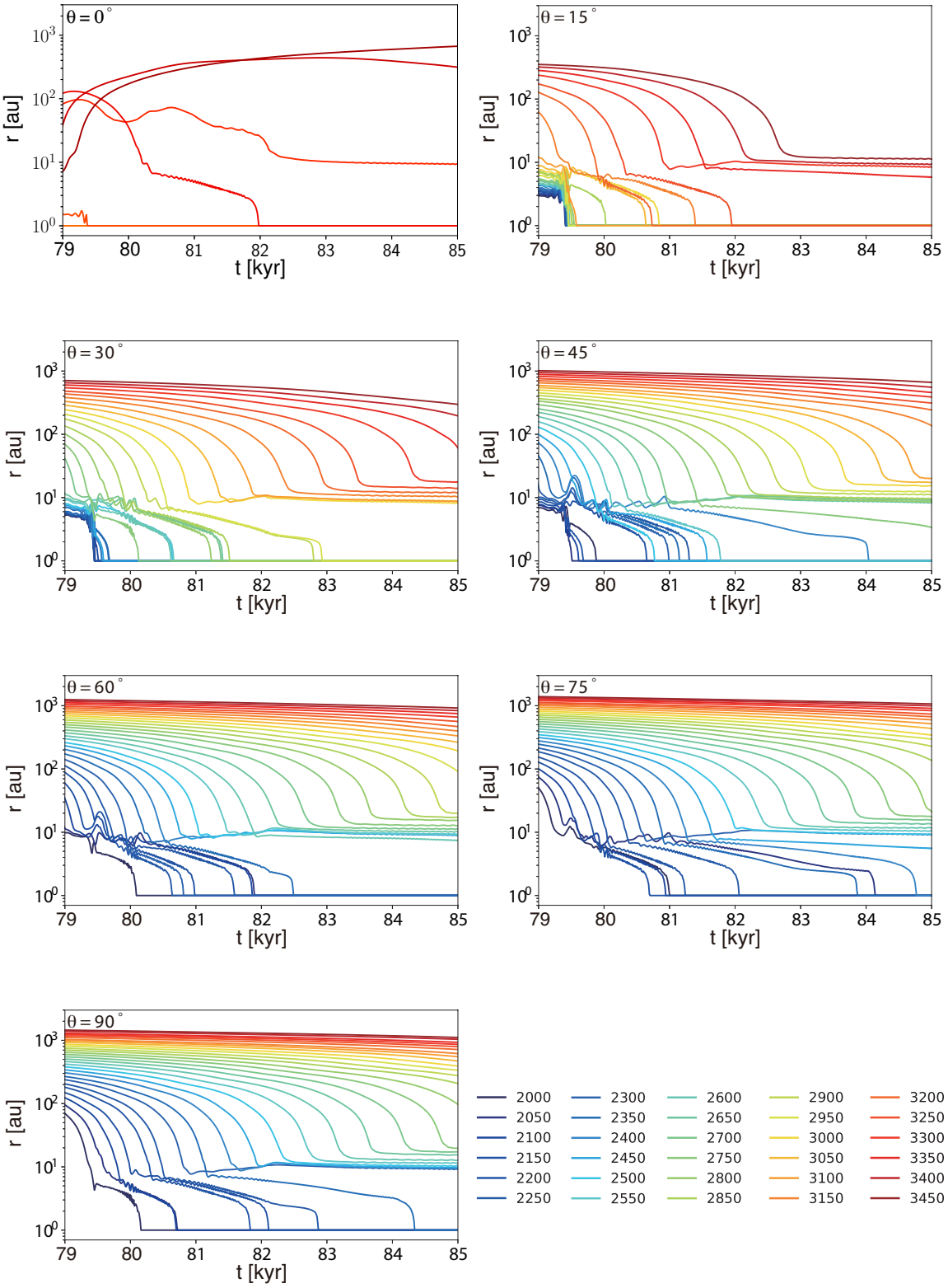

Figure 24: The same as in Fig.23 but with a dust particle size of $a_{\rm d}$ = 1000 μm.

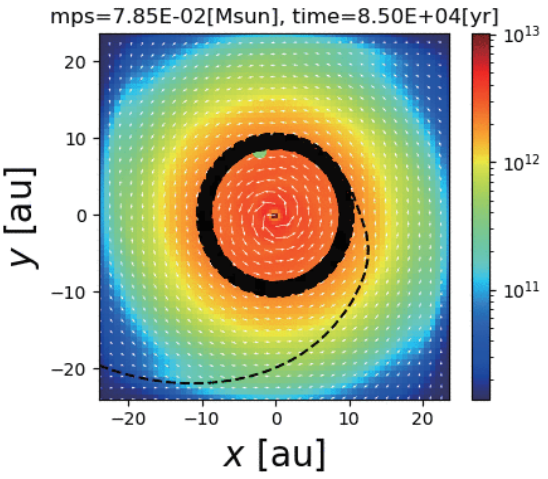

Figure 25: Trajectory of a dust particle with initial position $r = 1500$ au, $\theta = 90°$, and $a_{\rm d} = 0.01$ μm is plotted by the dotted black line. The gas number density (color) and velocity (arrows) on the $z = 0$.

at $r = 10$ au. In other words, it is probable that the condition required to keep the particles rotating at $ \$ r \$ $ = 10 au without falling is that they come from farther out than $r = 10$ au on the equatorial plane of the disk.

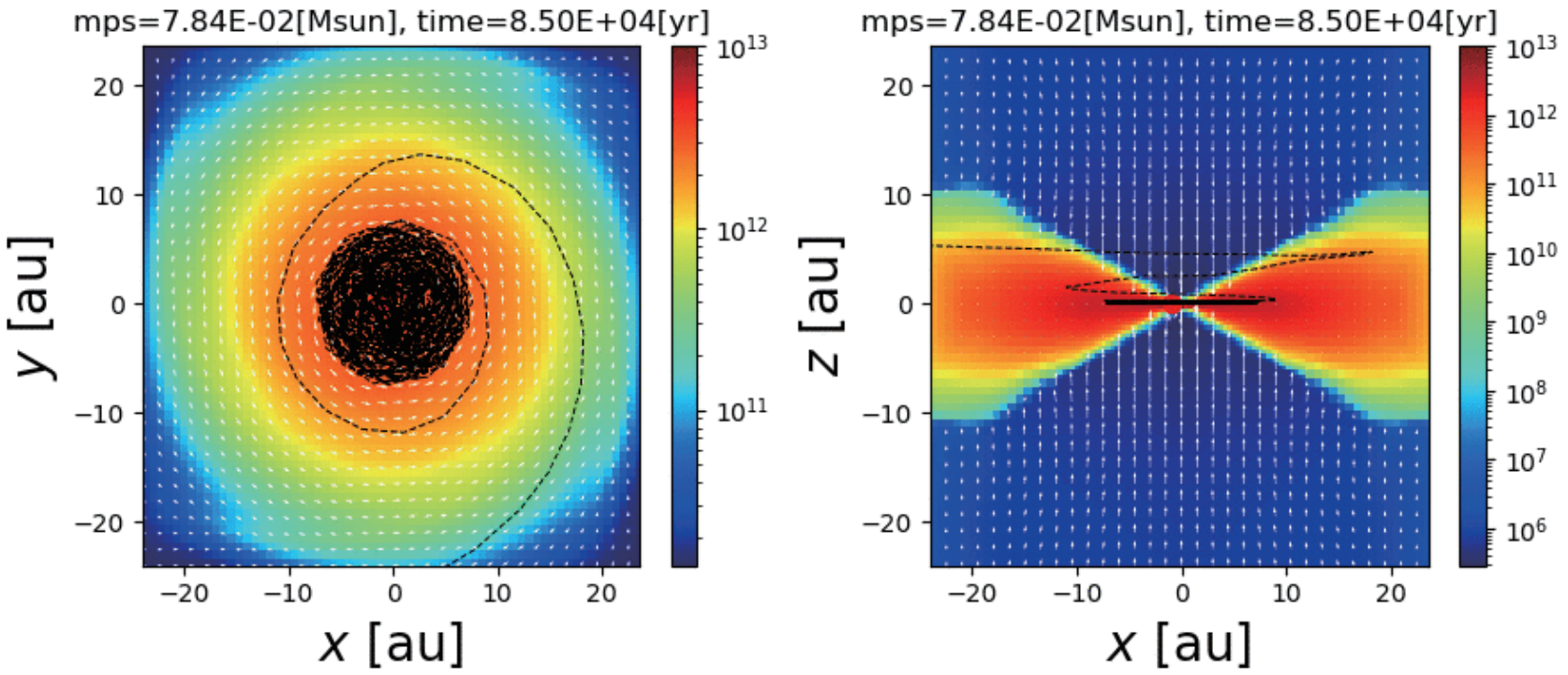

Figure 26: Trajectory of a dust particle with an initial position of $r = 1900$ au, $\theta = 45°$, and $a_{\rm d} = 0.01$ μm is plotted by the dotted black line. The gas number density (color) and velocity (arrows) on the $z = 0$ (left) $y = 0$ (right).

3.7 Dust coupling in the disk

In section §3.6, I provided the results of dust trajectories that have not been found in conventional planet formation models. In the following sections, the physical causes of such trajectories are discussed. In this section, I investigate whether or not dust particles that accrete from the equatorial plane onto the disk and rotate are coupled with gas. If the dust and the gas are strongly coupled in the disk, the gas is moving strongly, and the reason why dust particles rotate while maintaining a $r = 10$ au distance can be attributed to the gas movement. In §3.5, the Stokes number is defined as the free-fall timescale normalized by the stopping time. Fig. 22 shows that dust particles with $a_{\rm d} \geq 100\mu$m satisfy St ~ 1 while moving in the gas envelope and that the smaller particles are coupled with the gas. In the rotationally supported disk, dust particles that have the same size tend to be more strongly coupled with the gas than in the envelope due to the higher gas density. It should be noted that, hereafter, the Stokes number adopted in this study is defined differently from that defined in §2.3.2 and §3.5 because the free-fall time scale is not suitable for use as a dynamical time scale in a disk. More specifically, hereafter, St is defined as

$$\mathrm{St} = t_{\rm s}/t_{\rm K}, \tag{29}$$

where $t_{\rm K}$ is the Kepler time.

Fig. 27, 28 show the Stokes number time evolution for dust particles rotating in the disk with $a_{\rm d} = 0.01, 1000$ μm. The disk region is defined in 3.1 as the region where the rotational motion is dominant ($v_\phi > 2|v_r|$) and the gas is rotationally supported to some extent ($v_\phi > 0.6\, v_{\rm K}$, where $v_{\rm K}$ is the Keplerian velocity). Broken lines indicate dust particles that exist outside the disk region. For example, the line is temporarily broken while St is decreasing because the particles move into the envelope region. On the other hand, the fact that St starts to increase and then the line breaks indicates that the dust particle has accreted onto the sink particle. The forceful St increase is caused by the sudden decrease in r.

As shown in Fig. 27, dust particles entering and rotating in the disk from the envelope satisfy St < 1. In particular, dust particles with a circular motion at $r = 10$ au satisfy St $\sim 10^{-9}$ and are strongly coupled with gas. In Fig. 28, I plot the St time evolution with

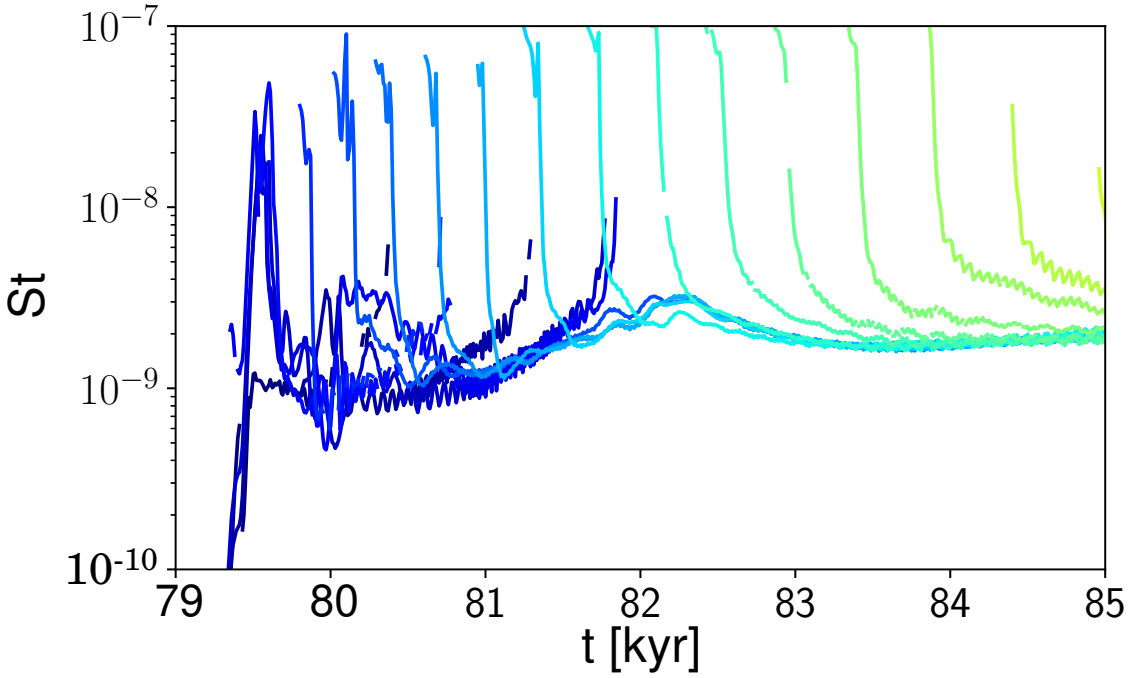

Figure 27: Time evolution of Stokes number for dust particles with $a_{\rm d}$ = 0.01 μm. St is defined in equation (29). Lines are only plotted when the particles are moving in the region defined as the disk according to §3.1. The colors used are the same as those used in Fig. 23.

$a_{\rm d}$ = 1000 μm, which is the maximum dust particle size prepared for this calculation. When dust particles are in the same physical state as gas, larger dust particles tend to be decoupled more easily from gas due to their longer stopping time. However, even a dust particle with $a_{\rm d}$ = 1000 μm satisfies St $\sim 10^{-4}$ and couples with gas when it is rotating in the disk. The St for particles with $a_{\rm d}$ = 1000 μm is five orders of magnitude larger than that for dust particles with $a_{\rm d}$ = 0.01 μm since St $\propto a_{\rm d}$. Taken together, I can conclude that the reason why some dust particles are rotating instead of gradually falling toward the central star is that the moving gas from the equatorial plane itself prevents the dust from accreting onto the central star and that the dust is controlled by gas motion.

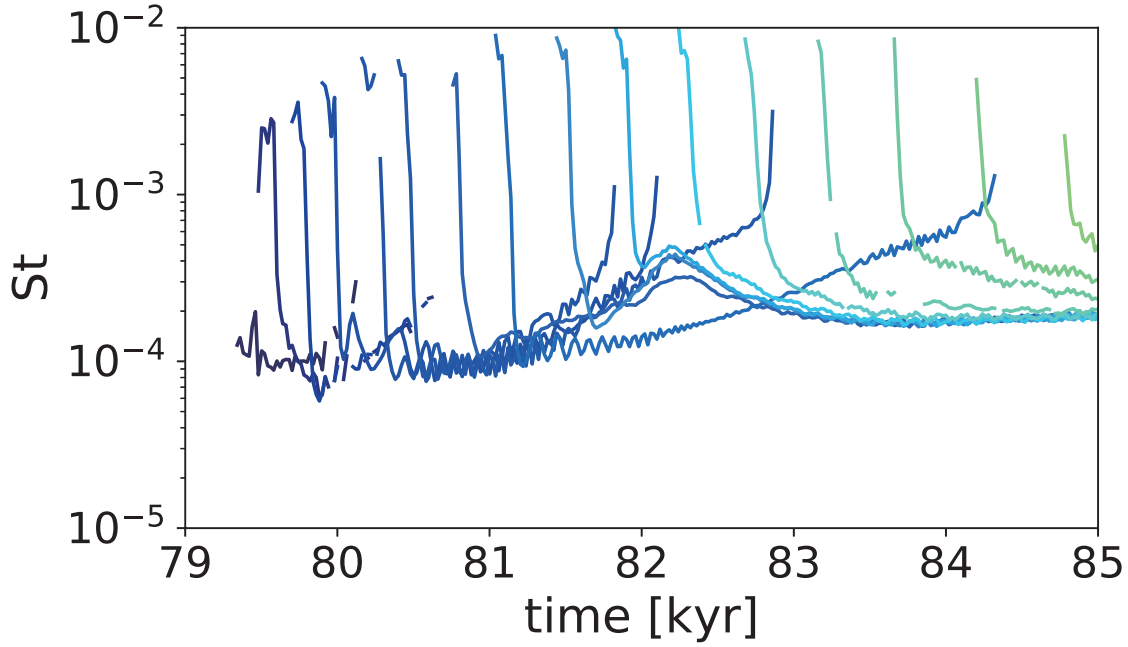

Figure 28: The same as in Fig. 27 but with a dust particle size of $a_{\rm d}$ = 0.01 μm. The colors are the same as those used in Fig. 24.

4 Discussion

4.1 Angular momentum transport via gravitational instability

In §3.7, it is shown that the dust particles moving in the disk are coupled with gas since the gas density is sufficiently high. Therefore, it is important to focus on the physical structure of the gas in order to investigate the cause of the rotating dust seen at r = 10 au that occurs without falling. In this section, I analyze the physical structure of the gas disk in the central region and discuss the rotating gas.

First, I focus on angular momentum transport in the disk. Fig. 29 shows that the local high-density region forms a spiral arm structure at a spatial scale of 10 au. The plotted time and spatial scales are the same as those shown in the bottom left of Fig. 10. However, in Fig. 29, the density color range is stricter to emphasize the spiral-arm structure. Previous studies have argued that gravitational instability is the trigger for the formation of regions with such predominant spiral modes. Since a high-density spiral arm is a nonaxisymmetric structure, angular momentum transport by gravitational torque becomes dominant in such regions.

To quantitatively evaluate the gravitational instability of gas, Toomre's Q value is adopted as defined in §3.1. In Fig. 30, the Q value is plotted in color on the equatorial plane. The region of 7 au $\leq r \leq$ 10 au satisfies Q < 2 and indicates that the existence of the spiral arm shown in Fig. 29 is due to gravitational instability. Inside r = 10 au, the angular momentum transport caused by gravitational torque causes the gas to lose angular momentum and fall into the central star. In contrast, outside at r = 10 au, the gas gains angular momentum and moves further outward. Thus, the gas at r = 10 au would move in a circular motion while maintaining its angular momentum. And, as shown in Fig. 23 - 26, dust particles that are strongly connected with the gas would have similar motions.

Next, by analyzing the specific angular momentum of the particles, I can determine whether or not the mechanism described above is reasonable. In Fig.31, I plot the time evolution of the specific angular momentum for the same two dust particles shown in Fig. 25

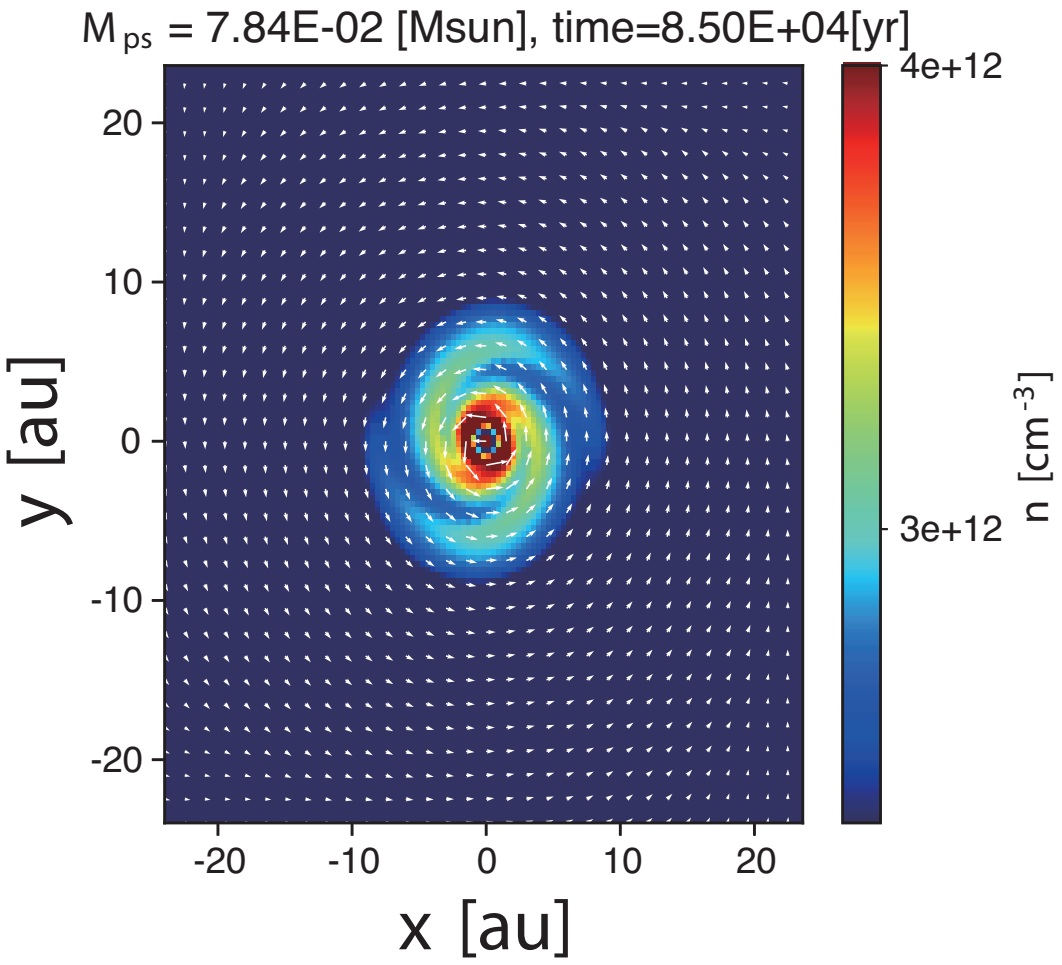

Figure 29: The same as bottom left panel in Fig. 10 but the color range indicating the gas number density is different.

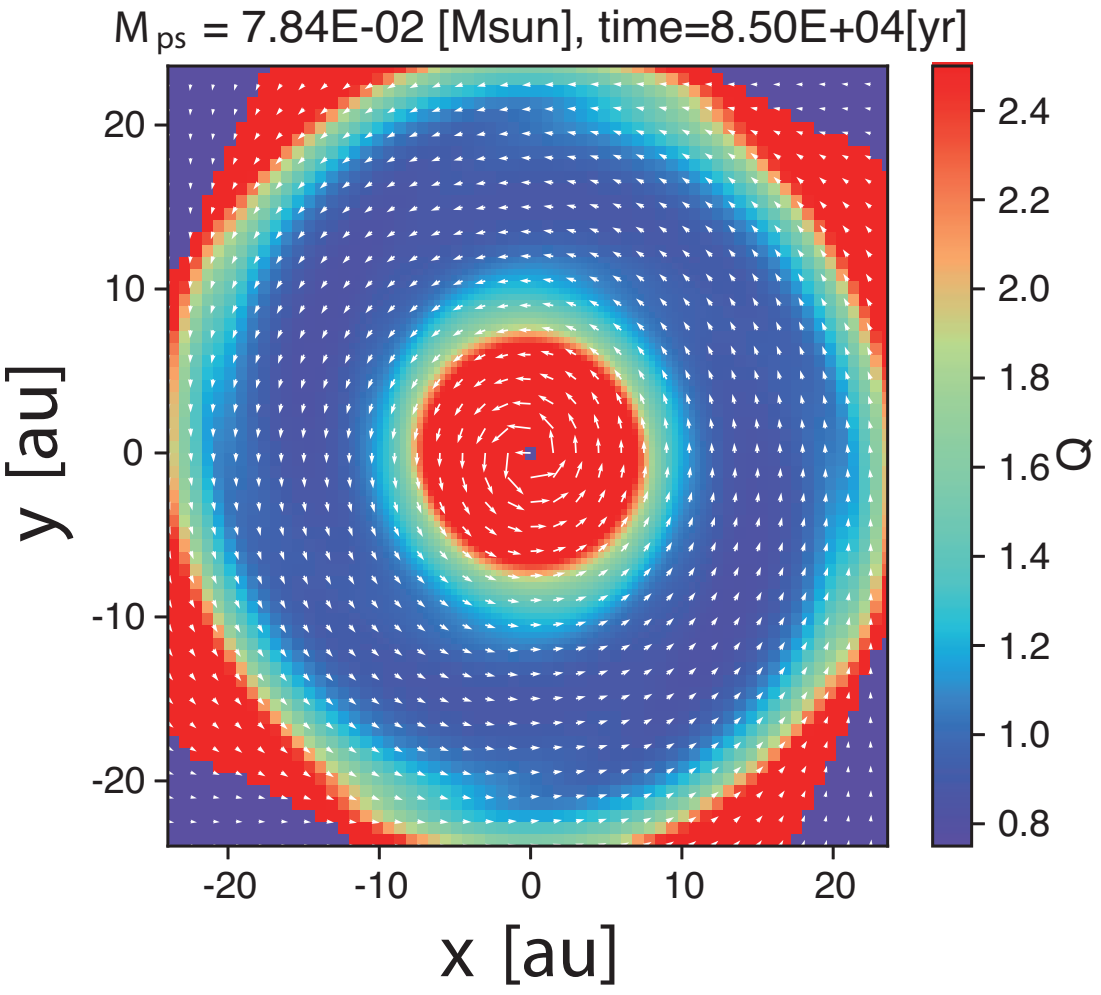

Figure 30: Toomre's Q value plotted by color for $z = 0$.

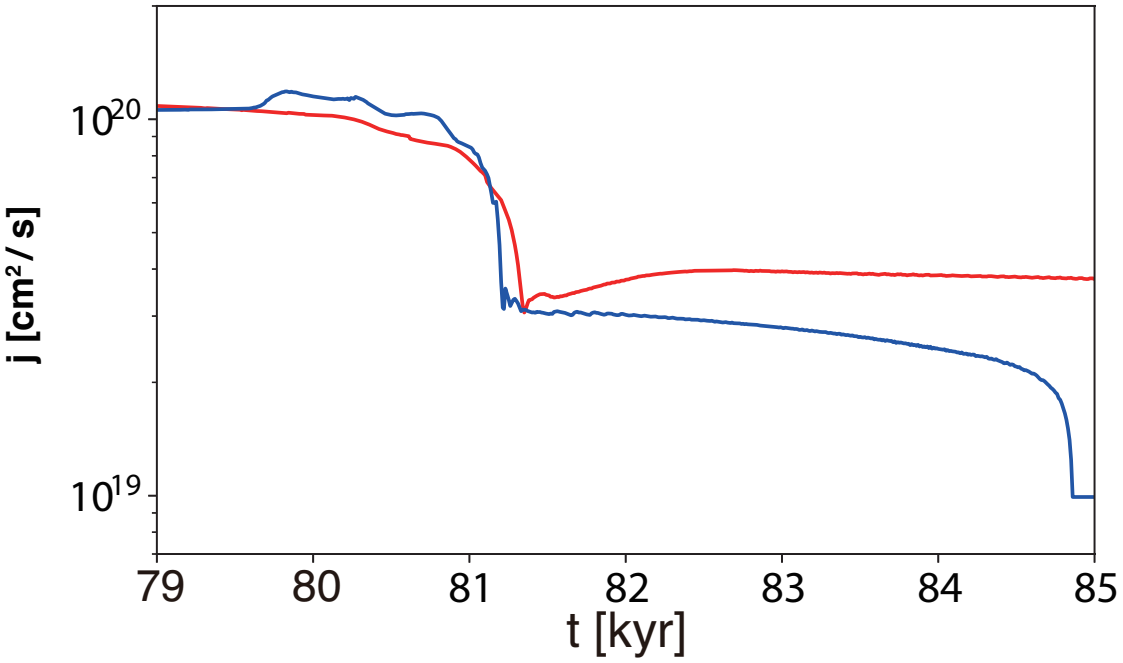

Figure 31: Specific angular momentum time evolution of two dust particles. The red line corresponds to a dust particle traveling with a circular motion at 10 au, as shown in Fig. 25. The blue line corresponds to a dust particle whose orbit is shown in Fig. 26, which is rotating within the disk and falling into the sink.

and 26. The dust particle falling into the sink (corresponding to the blue line) gradually loses its specific angular momentum in the disk. In contrast, the angular momentum of the dust particle rotating at $r = 10$ au (corresponding to the red line) remains constant.

Finally, the effect of magnetic fields is discussed. Plasma β is used to show whether or not the magnetic pressure is working. In Fig. 32, plasma $\beta = P/P_{\rm mag}$ is shown in color. In the rotating disk region with a spatial scale of 10 au, plasma $\beta \sim 10^5$. Thus, the effect of magnetic pressure on the gas dynamics in this region is negligible.

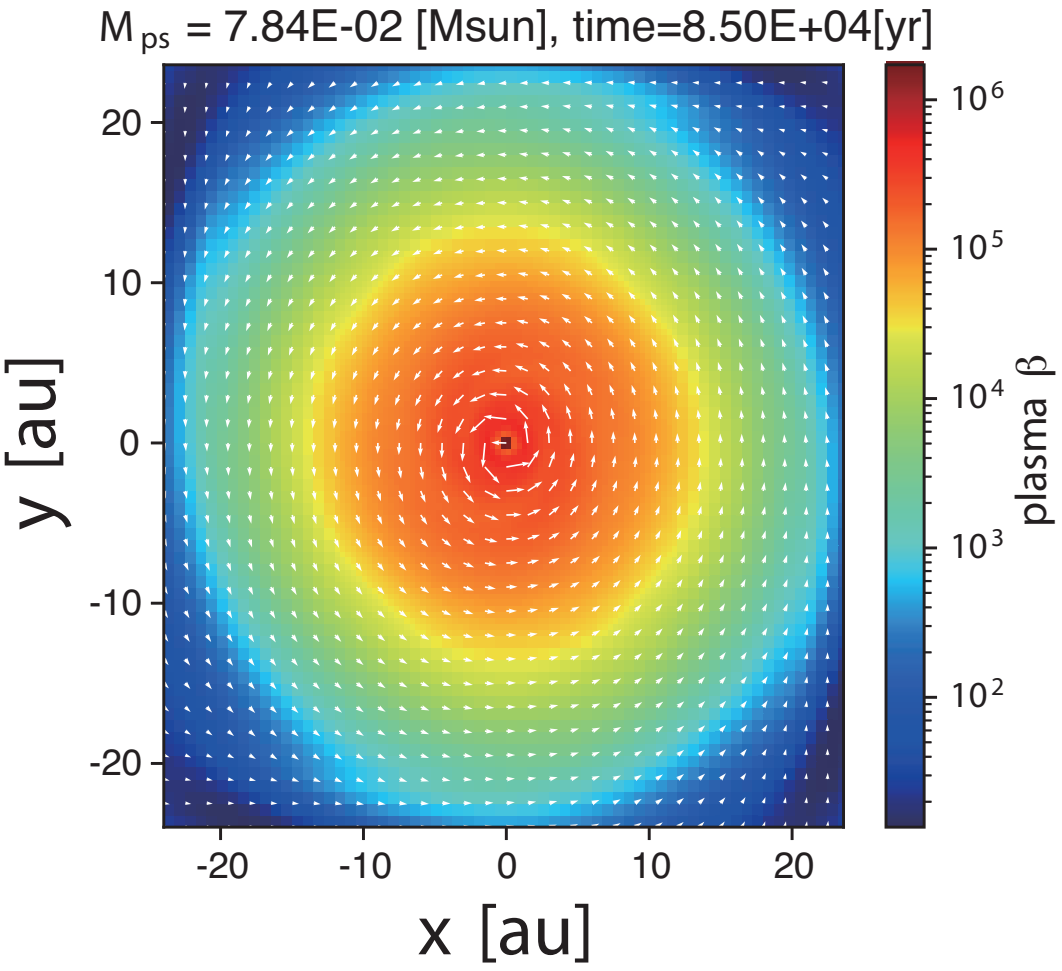

Figure 32: The same as in Fig. 30 but the color shows the plasma β.

4.2 Comparison with previous MHD simulations

Recently, Lebreuilly et al. (2020) investigated dust dynamics during the core collapse phase using 3D MHD simulations that introduced dust as a fluid. However, unlike the present study in which a sink cell was adopted as a protostar, that study did not use the sink method. Thus, there are some specific differences in the manner in which the dust and protostar are treated here. One significant difference is feedback from the dust to the gas (or the dust reaction back onto the gas). Although such feedback was not examined in this study, it is included in Lebreuilly et al. (2020), and our results are qualitatively and quantitatively in agreement with that study.

I also confirmed that dust concentration features seen in my study qualitatively agree with Lebreuilly et al. (2020). Specifically, that study reported that large dust particles partially decouple from the gas in the high-density regions near the disk and protostar (called fragments in Lebreuilly et al. 2020), and that dust depletion can be seen in the low-density regions of the outflow and envelope. My results are also quantitatively consistent with Lebreuilly et al. (2020), in which dust particles exceeding 10 μm are decoupled from the gas in the early star and disk formation processes.

Strictly speaking, a difference between this study and the above-mentioned study in terms of changes to the dust-to-gas mass ratio ($\delta f_{\rm dg}$ is described as ϵ in Lebreuilly et al. 2020). However, the $\delta f_{\rm dg}$ difference between them is a factor of 2-3, at most. For example, dust with a particle size of 100 μm is enhanced by a factor of about 3 (i.e., $\delta f_{\rm dg} = 3$) in the disk. On the other hand, in my calculation, the change of the dust-to-gas mass ratio is $\delta f_{\rm dg} = 1.2$, at most. Thus, $\delta f_{\rm dg}$ in my study is about 2.5 times smaller than that in Lebreuilly et al. (2020).

One possible reason for this might be differences in the initial gas distribution or gas mass density. Even though the gas density of my initial gas sphere is about 1-2 orders of magnitude lower than that of Lebreuilly et al. (2020), when the gas density is low, I found that dust particles tend to become decoupled from the gas. It is difficult to precisely explain why my results show a lower dust concentration compared with Lebreuilly et al.

(2020). Other possible reasons for the difference include the magnetic field strength (or mass-to-flux ratio) or the angle between the rotational angular velocity and the magnetic field. The inclusion of feedback from dust may also affect the results. As described below, there are numerous factors determining the dust-to-gas mass ratio, but the rough agreement between these studies indicates that dust decoupling becomes significant when the dust particles are $a_{\rm d} \gtrsim 10 - 100\,\mu$m in size.

4.3 Effects of dust properties on non-ideal MHD resistivities

A number of previous studies have examined the effects of dust properties on star formation processes in terms of non-ideal MHD properties (Dzyurkevich et al., 2017; Koga et al., 2019; Marchand et al., 2016; Tsukamoto et al., 2020; Zhao et al., 2018, 2021, 2016). These studies considered chemical networks including gas molecules and dust particles, and calculated the resistivities of non-ideal MHD effects. However, although they discussed the influences of the dust properties on the star formation processes using numerical simulations and analytical calculations, they did not consider relative velocities between the gas and dust. In contrast, this study showed that dust particles with $a_{\rm d} \leq 1\,\mu$m, which cover the MRN size distribution, are coupled with gas during star formation. Thus, relative velocities would not significantly change the resistivities as long as the dust particle sizes are smaller than $\lesssim 1\,\mu$m.

Recently, Guillet et al. (2020) showed that dust particle sizes could reach $10\,\mu$m even when the MRN size distribution is given as the initial distribution of the dust particles using one-dimensional (1D) gas evolution calculations that include ambipolar diffusion and turbulence. In particular, one of the most advanced aspects of Guillet et al. (2020) is the inclusion of charged particles (also see § 4.5) and their confirmation that dust growth can occur efficiently in particularly low-gas-density regions when the existence of charged dust particles and ambipolar diffusion are considered. (For details, see the Fig.8 of Guillet et al. 2020.) They also pointed out that the resistivities change significantly. My result indicates that the maximum dust particle size coupled with the gas is $10\,\mu$m. Thus, it is possible

that dust clustering in the high gas density region could change the resistivities. However, Guillet et al. (2020) did not include the porosity or the dust fragmentation process, which is important because these complicated processes will change the description of the relationship between dust and magnetic fields, as described in section 5.1 of Guillet et al. 2020. Accordingly, a refitment treatment of dust particles will be necessary to ensure that magnetic resistivities are understood correctly.

4.4 Charged dust dynamics

Although Tsukamoto et al. (2021a) investigated the behavior of charged dust in star formation simulations in great detail, this study assumes that dust is electrically neutral, even though the densities range and temperature levels present during star formation processes would ensure that sub-μm dust particles are negatively charged. (For details, see Draine & Sutin 1987.) Therefore, in order to treat the dust dynamics more realistically, it will be necessary to consider dust charge more thoroughly. Tsukamoto et al. (2021a) discussed the difficulty of simulating the evolution of charged dust particles, particularly in numerical simulations with a two-fluid approximation of the dust and gas fluids. Although a two-fluid approximation was not used in this study, the same problem arises. Fig. 11 in Tsukamoto et al. (2021a) compared the magnitude of the electric current generated by charged dust motion with that produced by gas particles (e.g., electrons). The figure also shows that the current generated by charged dust dominates that produced by the gas (or electron) driven current when the charged dust particle size is within the range of $\leq 1\mu$m and is embedded in a low-density region with a strong magnetic field, such as the outflow region. In this calculation, the current produced by charged dust $\boldsymbol{J}_{\rm d}$ cannot be simply defined as $\rho_{\rm d}$ because the dust particles are treated as discrete particles. However, $\boldsymbol{J}_{\rm d}$ may be dominant especially in the outflow region. Thus, the assumption that the total current $\boldsymbol{J} = \boldsymbol{J}_{\rm d} + \boldsymbol{J}_{\rm g} \approx \boldsymbol{J}_{\rm g}$ (where $\boldsymbol{J}_{\rm g}$ is the current produced by the charged gas) was not confirmed. This means that the spatial and time evolution of the magnetic field cannot be precisely calculated using the induction equation of the gas fluid (eq. (3)). As stated above, since the dust is assumed to be electrically neutral in this study, the above problems do not arise.

4.5 Dust growth in the star formation process

As described in §1, dust growth resulting from collisions should be considered using dust dynamics. Currently, dust growth in the star formation process is primarily treated using 1D gas evolution calculations (Guillet et al., 2020; Silsbee et al., 2020). Additionally, while Tsukamoto et al. (2021b) included the dust growth process in their 3D MHD simulations, the dust size evolution was calculated with a single-size approximation that ignored the size distribution. Furthermore, although the particle size evolution used in Tsukamoto et al. (2021b) may be valid, appropriate size distribution evolution is inevitably needed when calculating the chemical reaction and porosity that would significantly affect, for example, the resistivities of non-ideal MHD effects and dust growth connected with planet formation processes. It should also be noted that the dust size distribution and porosity can affect the dust opacity level. (For details, see Ormel et al. 2011, 2009.)

Very recently, Marchand et al. (2021) proposed the new method for calculating the distribution of dust particle growth that uses the Lagrangian history of a dust particle (or trajectory of a particle). However, their method only considered the collision rate for the gas turbulence proposed by Ormel & Cuzzi (2007). In their method, the manner in which dust particles are coupled with gas eddies is determined by the dust particle size, and the relative velocity is obtained from colliding particles with different sizes.

5 Summary

In this study, I presented a method for calculating the trajectories of dust particles in which the local physical gas quantities of gas fluid were used to calculate dust dynamics and treated the dust particles as Lagrangian particles. I then implemented the method using previously-existing nested grid code developed by my laboratory. Next, I executed a 3D MHD simulation that included the trajectory calculation for dust particles and investigated dust dynamics in a collapsing cloud with different-sized dust particles. The obtained results agree qualitatively and quantitatively with previous studies adopted as two- or one-fluid approximations with the Eulerian approach. It was also found that dust particles satisfying $a_{\rm d} \leq 10\,\mu$m are coupled with gas during gravitational collapse, at least until the protostellar mass reaches about 8% of the initial cloud core mass. This coupling condition is consistent with previous studies. The results obtained also showed that the trajectory calculation adopted in this study is an appropriate method for tracing the dust dynamics in star formation processes.

It was determined that some of the dust particles are swept up by the gas outflow, but dust particles initially located in the range of $0^\circ \leq \theta \leq 45^\circ$ are preferentially ejected by the outflow. On the other hand, dust particles $60^\circ \leq \theta \leq 90^\circ$ in size fall into the disk, move within it, and can grow to planetesimals because of collisions. Unlike small particles ($a_{\rm d} \leq 100\,\mu$m), dust particles $a_{\rm d} \geq 100\,\mu$m in size are decoupled from the gas fluid. In particular, dust particles $1000\,\mu$m in size are seldom captured by the outflow and readily fall into the disk. This phenomenon was also confirmed by the time evolution of $\delta f_{\rm dg}$, which is the enhancement factor of the dust-to-gas ratio normalized by the initial value $f_{\rm dg}$. The $\delta f_{\rm dg}$ value for dust particles $a_{\rm d} = 1000\,\mu$m in size significantly increases with time in the high-density gas region, thus indicating a significant enhancement of gas–dust coupling.

Dust particles with sizes of $a_{\rm d} \geq 100\,\mu$m are only decoupled from the gas when they are moving in low-density gas regions (i.e., the envelope and outflow). In contrast, in the rotationally supported disk, even dust particles that are $a_{\rm d} = 1000\,\mu$m in size, which is the largest dust particle adopted in this study, become coupled with gas because of the high gas density. I focused on the trajectories of the dust particles in the disk and found that

particles with an initial large θ (θ is the zenith angle) enter the disk from the equatorial plane rather than from the above and that such dust particles do not fall spiral down into the central star. Instead, they move in a circular motion without falling. Furthermore, I found that gas within 10 au loses its angular momentum while gas beyond 10 au receives angular momentum from the gravitational torque induced by the spiral-arm structure. Thus, at a distance of around 10 au, dust particles that are strongly coupled with gas will continue to move with a circular motion without falling.

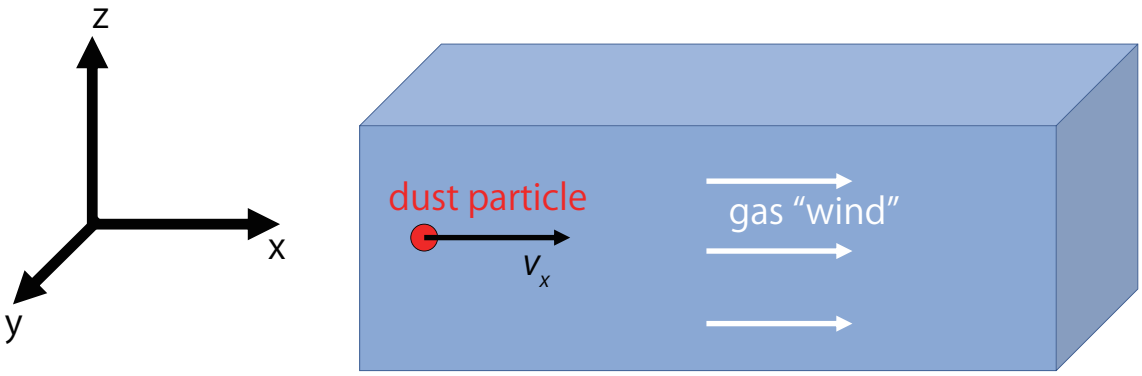

Figure 33: The schematic figure of the setting of the numerical test calculation.

Appendix : Numerical test calculation

To verify that the dust trajectory calculation is done correctly, some test calculations are performed. I introduce the details in this appendix.

I prepare the calculation region as a box, which has a uniform gas density, and there is to be assumed no gravity. Fig. 33 shows the schematic figure of the setting of the numerical test calculation. A dust particle is distributed in the box and uniform gas velocity is set along the x direction. Thus, the dust particle moves in the gas "wind". Initially, the gas velocity $\boldsymbol{v} = (v_g,\ 0,\ 0)$, where v_g is set below. The dust particle moves only with the x direction and test calculations are performed in 1D. To confirm the dust trajectory calculation is performed correctly, I compare the time evolution of the velocity of the dust particle with the analytical solution. In this appendix, three different test settings are provided.

Test 1 ; No external force

First, I set the simplest setting, in other words, a dust particle feels only the gas drag and no external force. Thus, the particle moves according to the equation of motion as

$$\frac{dv_x}{dt} = -\frac{v_x - v_{\rm g}}{t_{\rm s}}, \tag{30}$$

where v_x and $t_{\rm s}$ are the x velocity of the dust particle and the stopping time defined in equation (17), respectively. Numerical calculation is performed by the method described

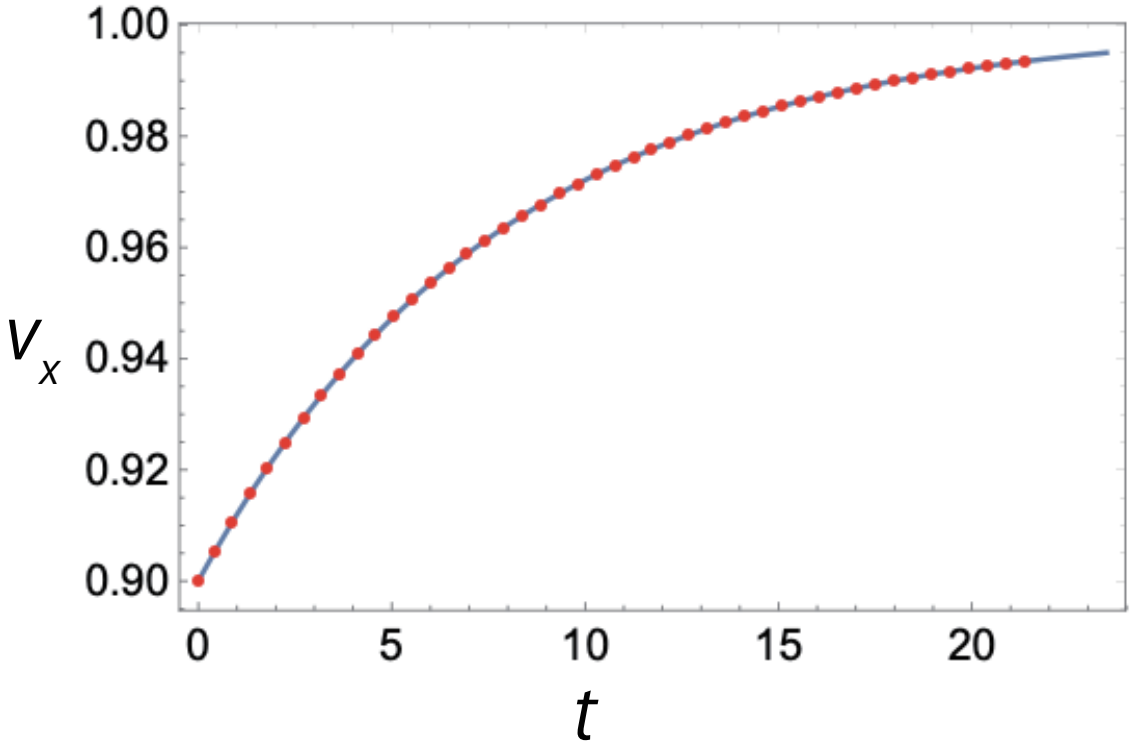

Figure 34: The time evolution of the velocity of the dust particle in Test1. The red points shows the results of the numericla calculation and the analytical solutions defined by equation (31) are plotted by red filled circles.

in §2.2.

To obtain the analytical solution, equation (30) is integrated with time and I acquire the solution

$$v_x = v_g + (v_g - v_0)e^{-\frac{t}{t_s}}, \tag{31}$$

where v_0 is the initial velocity of the dust particle. In this test, the parameters are set as $t_s = 7.82694$, $v_g = 1.0$ and $v_0 = 0.9$.

Fig. 34 plots the result of the test calculation in this setting. The dust trajectory numerical calculation well reproduces the analytical solution.

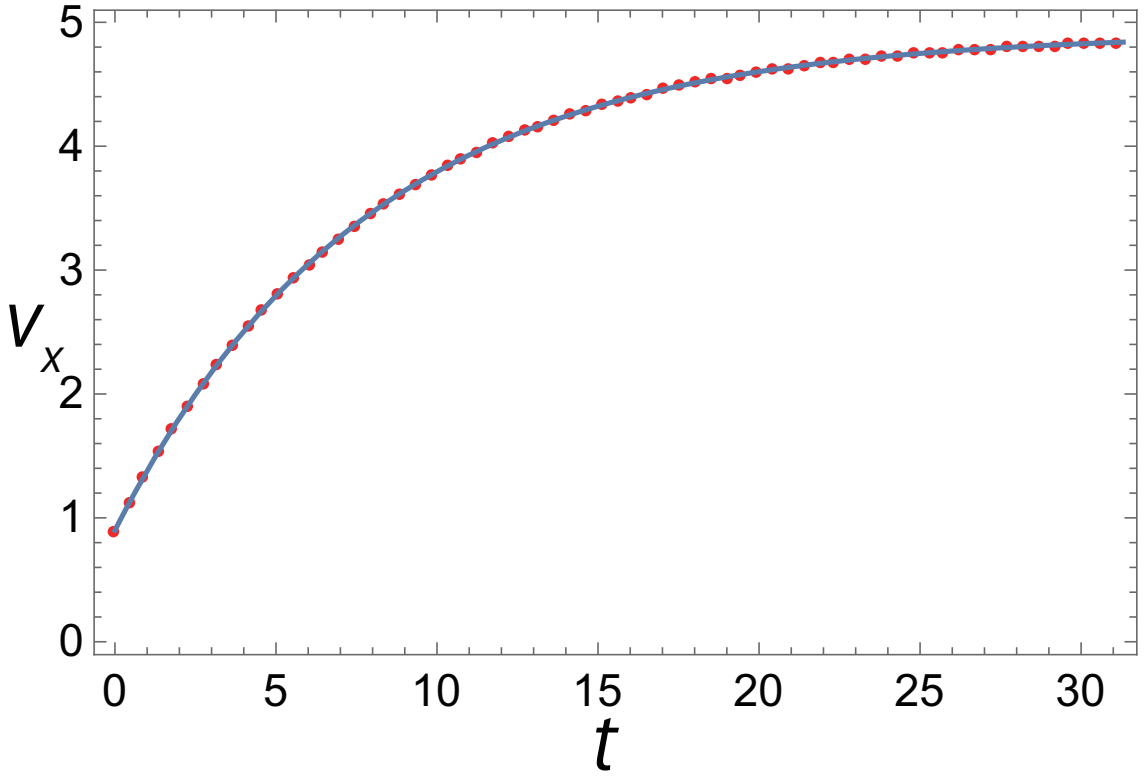

Figure 35: Same as Fig. 34 but the settings are adopted in Test2.

Test 2 ; Constant external force

Here, I add the external force to the setting of Test1. The equation of motion of the particle is described as

$$\frac{dv_x}{dt} = -\frac{v_x - v_{\rm g}}{t_{\rm s}} + b, \tag{32}$$

where b is introduced as the constant external force. The analytical solution is described as

$$v_x = (1 + t_{\rm s} b)\, v_{\rm g} + \Big(v_0 - (1 + t_{\rm s} b)\Big) e^{-\frac{t}{t_{\rm s}}}, \tag{33}$$

b is set as $b = 0.5$ and other parameters are same as defined in Test1.

Fig. 35 plots the result of the test calculation in this setting. The dust trajectory numerical calculation well reproduces the analytical solution.

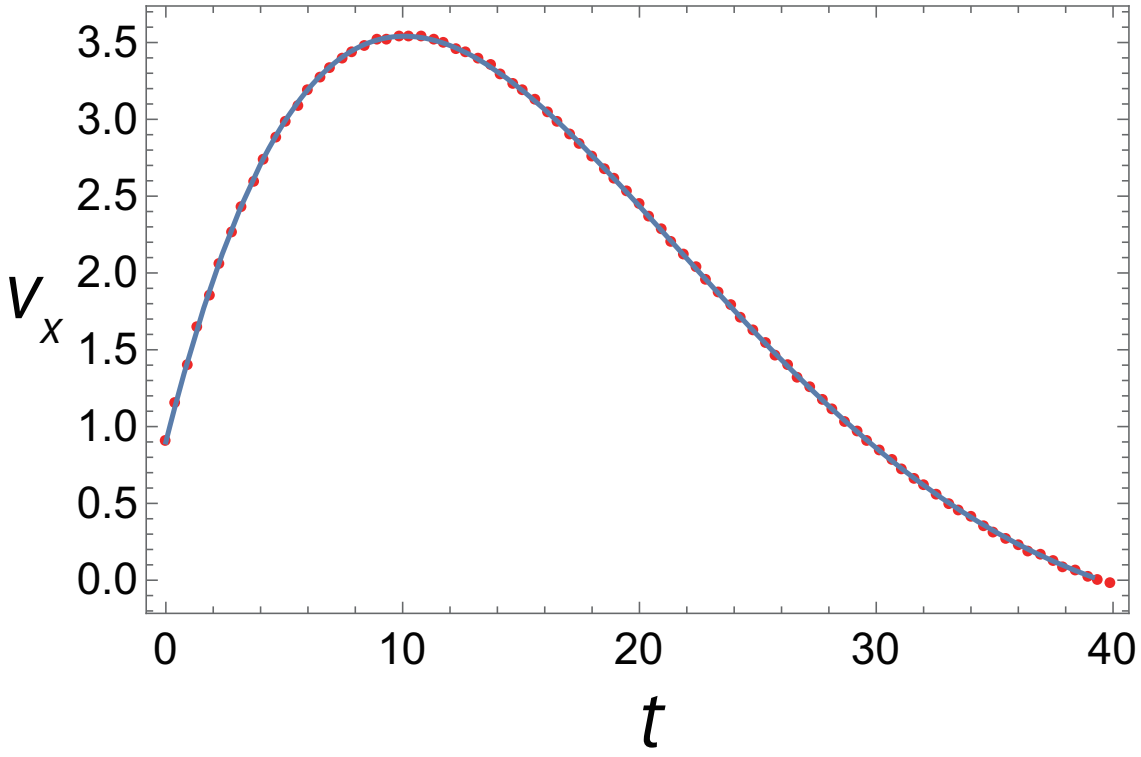

Figure 36: Same as Fig. 34 but the settings are adopted in Test3.

Test 3; External force depending on the location

Moreover, I introduce the external force depending on the x coordinate instead of the constant value adopted in Test2. The equation of motion of the particle is described as

$$\frac{dv_x}{dt} = -\frac{v_x - v_{\rm g}}{t_{\rm s}} + bx, \tag{34}$$

where x_0 is defined as the initial position of the dust particle. The analytical solution is described as

$$\begin{aligned} v_x &= -\frac{t_{\rm s} v_0}{2}\left(-\frac{1}{t_s} - \sqrt{\frac{1}{t_s^2} + 4b}\right) e^{\frac{1}{2}\left(-\frac{1}{t_s} - \sqrt{\frac{1}{t_{\rm s}^2}+4b}\right)t} \\ &- \frac{v_0 v_{\rm g} - b x_0}{2b}\left(-\frac{1}{t_s} + \sqrt{\frac{1}{t_s^2} + 4b}\right) e^{\frac{1}{2}\left(-\frac{1}{t_s} + \sqrt{\frac{1}{t_{\rm s}^2}+4b}\right)t}, \end{aligned} \tag{35}$$

where b and x_0 are set as $b = -0.01$ and $x_0 = -60.0$, respectively.

Fig. 36 plots the result of the test calculation in this setting. The dust trajectory numerical calculation well reproduces the analytical solution.

Acknowledgements

First and foremost, I wish to thank my supervisor, Associate Professor Masahiro Machida, for his steadfast support as I conducted my research. I would also like to thank everyone for providing me with so many useful comments in relation to my research, and I am especially grateful to my fellow lab members for the discussions I held on a daily basis. Additionally, I would also like to thank my family for their support over the course of my life. This research used the computational resources of the High-Performance Computing Infrastructure (HPCI) system provided by the Cyberscience Center at Tohoku University, the Cybermedia Center at Osaka University, and the Earth Simulator at the Japan Agency for Marine-Earth Science and Technology (JAMSTEC) through the HPCI System Research Project (Project IDs: hp190035, hp200004, and hp210004). The simulations reported in this paper were also performed in 2020 and 2021 by Koubo Kadai on the Earth Simulator (NEC SX-ACE and NEC SX-Aurora Tsubasa supercomputers) at JAMSTEC.

References

Ansdell, M.., Williams, J. P.., van der Marel, N.., et al. 2016, ApJ, 828, 46, doi: 10.3847/0004-637X/828/1/46

Aso, Yusuke., & Machida, Masahiro N.. 2020, ApJ, 905, 174, doi: 10.3847/1538-4357/abc6fc

Bai, Xue-Ning., & Stone, James M.. 2010, ApJ, 722, 1437, doi: 10.1088/0004-637X/722/2/1437

Bate, Matthew R.., & Lorén-Aguilar, Pablo. 2017, MNRAS, 465, 1089, doi: 10.1093/mnras/stw2853

Beitia-Antero, Leire., Gómez de Castro, Ana I.., & Vallejo, Juan C.. 2021, ApJ, 908, 112, doi: 10.3847/1538-4357/abcda1

Brauer, F.., Dullemond, C. P.., & Henning, Th.. 2008, A&A, 480, 859, doi: 10.1051/0004-6361:20077759

Draine, B. T.., & Sutin, B.. 1987, ApJ, 320, 803, doi: 10.1086/165596

Dzyurkevich, Natalia., Commerçon, Benoît., Lesaffre, Pierre., & Semenov, Dimitry. 2017, A&A, 603, A105, doi: 10.1051/0004-6361/201628995

Epstein, Paul S.. 1924, Physical Review, 23, 710, doi: 10.1103/PhysRev.23.710

Flock, Mario., & Mignone, Andrea. 2021, A&A, 650, A119, doi: 10.1051/0004-6361/202040104

Furuya, Kenji., Aikawa, Yuri., Tomida, Kengo., et al. 2012, ApJ, 758, 86, doi: 10.1088/0004-637X/758/2/86

Galametz, M.., Maury, A. J.., Valdivia, V.., et al. 2019, A&A, 632, A5, doi: 10.1051/0004-6361/201936342

Guillet, V.., Hennebelle, P.., Pineau des Forêts, G.., et al. 2020, A&A, 643, A17, doi: 10.1051/0004-6361/201937387

Guzmán, Viviana V.., Huang, Jane., Andrews, Sean M.., et al. 2018, ApJ, 869, L48, doi: 10.3847/2041-8213/aaedae

Hayashi, C.. 1981, Progress of Theoretical Physics Supplement, 70, 35, doi: 10.1143/PTPS.70.35

Hayashi, C.., Nakazawa, K.., & Nakagawa, Y.. 1985, in Protostars and Planets II, ed. D. C. Black & M. S. Matthews, 1100–1153

Hennebelle, P.., & Fromang, S.. 2008, A&A, 477, 9, doi: 10.1051/0004-6361:20078309

Hildebrand, R. H.. 1983, QJRAS, 24, 267

Huang, Jane., Andrews, Sean M.., Dullemond, Cornelis P.., et al. 2018a, ApJ, 869, L42, doi: 10.3847/2041-8213/aaf740

Huang, Jane., Andrews, Sean M.., Pérez, Laura M.., et al. 2018b, ApJ, 869, L43, doi: 10.3847/2041-8213/aaf7a0

Isella, Andrea., Huang, Jane., Andrews, Sean M.., et al. 2018, ApJ, 869, L49, doi: 10.3847/2041-8213/aaf747

Johansen, A.., & Youdin, A.. 2007, ApJ, 662, 627, doi: 10.1086/516730

Joos, M.., Hennebelle, P.., & Ciardi, A.. 2012, A&A, 543, A128, doi: 10.1051/0004-6361/201118730

Koga, Shunta., Tsukamoto, Yusuke., Okuzumi, Satoshi., & Machida, Masahiro N.. 2019, MNRAS, 484, 2119, doi: 10.1093/mnras/sty3524

Kurtovic, Nicolás T.., Pérez, Laura M.., Benisty, Myriam., et al. 2018, ApJ, 869, L44, doi: 10.3847/2041-8213/aaf746

Kwon, Woojin., Looney, Leslie W.., Mundy, Lee G.., Chiang, Hsin-Fang., & Kemball, Athol J.. 2009, ApJ, 696, 841, doi: 10.1088/0004-637X/696/1/841

Laibe, Guillaume., & Price, Daniel J.. 2012, MNRAS, 420, 2365, doi: 10.1111/j.1365-2966.2011.20201.x

—. 2014, MNRAS, 440, 2147, doi: 10.1093/mnras/stu359

Lebreuilly, U.., Commerçon, B.., & Laibe, G.. 2020, A&A, 641, A112, doi: 10.1051/0004-6361/202038174

Lee, Chin-Fei., Hirano, Naomi., Zhang, Qizhou., et al. 2014, ApJ, 786, 114, doi: 10.1088/0004-637X/786/2/114

Li, Jennifer I-Hsiu., Liu, Hauyu Baobab., Hasegawa, Yasuhiro., & Hirano, Naomi. 2017, ApJ, 840, 72, doi: 10.3847/1538-4357/aa6f04

Machida, Masahiro N.., & Hosokawa, Takashi. 2013, MNRAS, 431, 1719, doi: 10.1093/mnras/stt291

Machida, M. N.., Inutsuka, S.-i.., & Matsumoto, T.. 2007, ApJ, 670, 1198, doi: 10.1086/521779

Machida, Masahiro N.., Inutsuka, Shu-ichiro., & Matsumoto, Tomoaki. 2010, ApJ, 724, 1006, doi: 10.1088/0004-637X/724/2/1006

Machida, M. N.., & Matsumoto, T.. 2011, MNRAS, 413, 2767, doi: 10.1111/j.1365-2966.2011.18349.x

Machida, Masahiro N.., & Matsumoto, Tomoaki. 2012, MNRAS, 421, 588, doi: 10.1111/j.1365-2966.2011.20336.x

Machida, Masahiro N.., Tomisaka, Kohji., & Matsumoto, Tomoaki. 2004, MNRAS, 348, L1, doi: 10.1111/j.1365-2966.2004.07402.x

Marchand, P.., Guillet, V.., Lebreuilly, U.., & Mac Low, M. M.. 2021, A&A, 649, A50, doi: 10.1051/0004-6361/202040077

Marchand, P.., Masson, J.., Chabrier, G.., et al. 2016, A&A, 592, A18, doi: 10.1051/0004-6361/201526780

Masson, J.., Chabrier, G.., Hennebelle, P.., Vaytet, N.., & Commerçon, B.. 2016, A&A, 587, A32, doi: 10.1051/0004-6361/201526371

Mathis, J. S.., Rumpl, W.., & Nordsieck, K. H.. 1977, ApJ, 217, 425, doi: 10.1086/155591

Miettinen, O.., Harju, J.., Haikala, L. K.., & Juvela, M.. 2012, A&A, 538, A137, doi: 10.1051/0004-6361/201117849

Miotello, A.., Testi, L.., Lodato, G.., et al. 2014, A&A, 567, A32, doi: 10.1051/0004-6361/201322945

Nakano, T.., Nishi, R.., & Umebayashi, T.. 2002, ApJ, 573, 199, doi: 10.1086/340587

Ormel, C. W.., & Cuzzi, J. N.. 2007, A&A, 466, 413, doi: 10.1051/0004-6361:20066899

Ormel, C. W.., Min, M.., Tielens, A. G. G. M.., Dominik, C.., & Paszun, D.. 2011, A&A, 532, A43, doi: 10.1051/0004-6361/201117058

Ormel, C. W.., Paszun, D.., Dominik, C.., & Tielens, A. G. G. M.. 2009, A&A, 502, 845, doi: 10.1051/0004-6361/200811158

Pagani, Laurent., Steinacker, Jürgen., Bacmann, Aurore., Stutz, Amelia., & Henning, Thomas. 2010, Science, 329, 1622, doi: 10.1126/science.1193211

Pérez, Laura M.., Benisty, Myriam., Andrews, Sean M.., et al. 2018, ApJ, 869, L50, doi: 10.3847/2041-8213/aaf745

Price, Daniel J.., & Bate, Matthew R.. 2007, MNRAS, 377, 77, doi: 10.1111/j.1365-2966.2007.11621.x

Sheehan, Patrick D.., Tobin, John J.., Federman, Sam., Megeath, S. Thomas., & Looney, Leslie W.. 2020, ApJ, 902, 141, doi: 10.3847/1538-4357/abbad5

Silsbee, Kedron., Ivlev, Alexei V.., Sipilä, Olli., Caselli, Paola., & Zhao, Bo. 2020, A&A, 641, A39, doi: 10.1051/0004-6361/202038063

Steinacker, J.., Andersen, M.., Thi, W. F.., & Bacmann, A.. 2014, A&A, 563, A106, doi: 10.1051/0004-6361/201323219

Steinacker, J.., Andersen, M.., Thi, W. F.., et al. 2015, A&A, 582, A70, doi: 10.1051/0004-6361/201425434

Tomida, Kengo., Machida, Masahiro N.., Hosokawa, Takashi., Sakurai, Yuya., & Lin, Chia Hui. 2017, ApJ, 835, L11, doi: 10.3847/2041-8213/835/1/L11

Tomida, K.., Okuzumi, S.., & Machida, M. N.. 2015, ApJ, 801, 117, doi: 10.1088/0004-637X/801/2/117

Tomida, K.., Tomisaka, K.., Matsumoto, T.., et al. 2013, ApJ, 763, 6, doi: 10.1088/0004-637X/763/1/6

Toomre, A.. 1964, ApJ, 139, 1217, doi: 10.1086/147861

Tsukamoto, Y.., Iwasaki, K.., Okuzumi, S.., Machida, M. N.., & Inutsuka, S.. 2015, MNRAS, 452, 278, doi: 10.1093/mnras/stv1290

Tsukamoto, Y.., Machida, M. N.., & Inutsuka, S.. 2021a, ApJ, 913, 148, doi: 10.3847/1538-4357/abf5db

Tsukamoto, Yusuke., Machida, Masahiro N.., & Inutsuka, Shu-ichiro. 2021b, arXiv e-prints, arXiv:2109.12779. https://arxiv.org/abs/2109.12779

Tsukamoto, Y.., Machida, M. N.., Susa, H.., Nomura, H.., & Inutsuka, S.. 2020, ApJ, 896, 158, doi: 10.3847/1538-4357/ab93d0

Uehara, Hayato., Dobashi, Kazuhito., Nishiura, Shingo., Shimoikura, Tomomi., & Naoi, Takahiro. 2021, ApJ, 915, 74, doi: 10.3847/1538-4357/ac03b4

Vorobyov, Eduard I.., Akimkin, Vitaly., Stoyanovskaya, Olga., Pavlyuchenkov, Yaroslav., & Liu, Hauyu Baobab. 2018, A&A, 614, A98, doi: 10.1051/0004-6361/201731690

Weidenschilling, S. J.. 1977, MNRAS, 180, 57, doi: 10.1093/mnras/180.2.57

Wurster, J.., Price, D. J.., & Bate, M. R.. 2016, MNRAS, 457, 1037, doi: 10.1093/mnras/stw013

Zhao, B.., Caselli, P.., & Li, Z.-Y.. 2018, MNRAS, 478, 2723, doi: 10.1093/mnras/sty1165

Zhao, Bo., Caselli, Paola., Li, Zhi-Yun., et al. 2021, MNRAS, 505, 5142, doi: 10.1093/mnras/stab1295

Zhao, B.., Caselli, P.., Li, Z.-Y.., et al. 2016, MNRAS, 460, 2050, doi: 10.1093/mnras/stw1124